Experimental Assessment and Model Validation of the SPARC Toroidal Field Model Coil

D. G. Whyte, B. LaBombard, J. Doody, T. Golfinopolous, R. Granetz, C. Lammi, S. Lane-Walsh, P. Michael, T. Mouratidis, R. Mumgaard, J. P. Muncks, D. Nash, N. Riva, F. Santoro, A. Sattarov, J. Stillerman, K. Uppalapati, R. Vieira, A. Watterson, S. Wilcox, and Z. S. Hartwig

***Abstract*—In this article, the SPARC Toroidal Field Model Coil (TFMC) experimental tests are described. The tests include detailed comparisons to a hierarchy of electromagnetic and structural models of the coil. The tests confirm the ability of the no-insulation no-twist (NINT) configuration to provide highly stable dc operations with peak magnetic field in excess of 20 T at the rare earth yttrium barium copper oxide (REBCO) tape stacks. The advantages of the modular TFMC approach are validated including the ability to test and probe the REBCO and structural response of the coil in stages, a strategy that will be applied to large-scale coil production for SPARC. The electromagnetic models show high fidelity agreement to the dc and charging coil performance in terms of current distribution, voltages, and heating. The transient response of the TFMC to open-circuit events is examined. The coil exhibits the positive features of the NINT design with very low induced voltages and a predictable redistribution of current and resulting volumetric heating. However, highly localized damage occurs during a programmed open circuit at operational conditions similar to those used in the SPARC tokamak, in agreement with calibrated electromagnetic models. This reveals the cause and remedy to the thermal instability that gives rise to the damage. Therefore, the conclusion of the tests is that the NINT TFMC is confirmed as meeting the programmatic requirements for SPARC and, more generally, for high-field tokamaks.**

***Index Terms*—Electromagnets, fusion reactors, superconducting magnets, tokamaks.**

I. Introduction

THE SPARC Toroidal Field Model Coil (TFMC) Project was an approximately three-year effort between 2018 and 2021 that developed novel rare earth yttrium barium copper oxide (REBCO) superconductor technologies [1], [2], [3], [4] and then utilized those technologies to successfully design, build, and test a first-in-class high-field (∼20 T) representative scale (∼3 m in linear size) superconducting toroidal field (TF) coil (see Table I). With the principal objective of retiring the design, fabrication, and operational risks inherent in large-scale no-insulation REBCO superconducting magnets for fusion energy devices, the project was executed jointly by the MIT Plasma Science and Fusion Center (PSFC) and Commonwealth Fusion Systems (CFS) as a critical technology enabler of the high-field pathway to fusion energy [5] and, in particular, as a risk retirement program for the TF magnet in the SPARC net-energy fusion tokamak [6]. The parties have pursued patent protection relating to inventions created from their research collaborations, and CFS has exclusive commercial rights to the technology for energy applications. This article is part of a collection of papers intended to cover the principal parts of the TFMC project, including the design and fabrication of the magnet, the design and assembly of the test facility, and an overview of the results from the experimental test campaigns carried out in the fall of 2021. The focus of this article is on the experimental testing of the TFMC and validation of computation models used to predict the TFMC performance.

TABLE I
Nominal TFMC Parameters

Overall magnet mass	10 058 kg
Overall magnet size	2.9 m × 1.9 m
WP mass	5 311 kg
WP current density	153 A/mm^2
WP inductance	0.136 H
WP amp-turns	10.4 MA-turns
Terminal current	40 kA
Number of turns	256
Number of pancakes	16
Total REBCO tape length	270 km
Coolant type	Supercritical He
Max. coolant pressure	25 bar
Operating temperature	20 K
Peak magnet field	20.3 T
Peak Lorentz loading	822 kN/m
Magnetic stored energy	110 MJ
"No-Insulation No-Twist" REBCO tape stacks	NINT

II. Model and Testing Descriptions

The no-insulation no-twist (NINT) design was chosen to meet the requirements of the SPARC TF coils. The principal requirement is to provide dc toroidal magnetic field with peak amplitude at or above 20 T, which allows SPARC to be compact

Manuscript received 18 August 2023; revised 12 October 2023; accepted 5 November 2023. Date of publication 14 November 2023; date of current version 7 December 2023. *(Corresponding author: D. G. Whyte.)*

D. G. Whyte, B. LaBombard, J. Doody, T. Golfinopolous, R. Granetz, S. Lane-Walsh, P. Michael, T. Mouratidis, N. Riva, F. Santoro, J. Stillerman, R. Vieira, A. Watterson, and Z. S. Hartwig are with the Plasma Science and Fusion Center, Massachusetts Institute of Technology, Cambridge, MA 02139 USA (e-mail: whyte@psfc.mit.edu).

C. Lammi, R. Mumgaard, J. P. Muncks, D. Nash, A. Sattarov, K. Uppalapati, and S. Wilcox are with Commonwealth Fusion Systems, Devens, MA 01434 USA.

Color versions of one or more figures in this article are available at https://doi.org/10.1109/TASC.2023.3332823.

Digital Object Identifier 10.1109/TASC.2023.3332823

yet achieve net energy gain and fusion power at a commercially relevant scale [6]. The technical challenges to be addressed by the TFMC must confirm that the REBCO superconductors and coil structure can tolerate simultaneously the high magnetic field and Lorentz forces of the SPARC TF. The eventual commercial use further required that the TF design and, hence, the TFMC meet the programmatic requirements of proven assembly and quality-control features, which would allow for large-scale repetition and replication in SPARC and future fusion power plants based on high field like affordable robust compact (ARC) [5]. The details of the TFMC NINT design are found in the companion papers [7], [8] and are briefly summarized. The coils consist of individual pancakes stacked together. Each pancake structure, made from high strength cryogenic steel, has one side where grooves are machined in a spiral pattern, largely azimuthal, that traverse the pancake radially from inside to outside. Stacks of REBCO tape are inserted into the grooves with the tape faces perpendicular to the radial direction (i.e., inserted on edge), with copper caps then inserted on the groove tops to act as electrical and structural stabilizers to the tape. The REBCO crystal sides of tapes were all on the radial inside such that the bending provides compression strain, thus counteracting the tensile strain from Lorentz loading. A vacuum pressure impregnation (VPI) process then fills any voids in the groove/tape/cap volume with solder, providing for greatly enhanced electrical and thermal connection and continuity between tapes. This entire system is called a tape "stack" and comprises the superconductor unit for NINT, and these azimuthal superconductor current pathways provide the ampere-turns. The other side of the pancake plate has cooling channels machined in a pattern to optimally distribute the supercritical helium. The coil is comprised of multiple pancakes stacked on each other to increase ampere-turns, such that the cooling and stack sides alternate with current continuity from pancake to pancake using resistive pressure joint primarily made of copper.

NINT was chosen over more traditional insulated cable-based conductor designs for several technical and programmatic reasons. The lack of insulator greatly simplifies the assembly process since after the VPI solder process, all that is required is mechanical assembly of the joint connections and insertion in the structural case. Each pancake can be individually tested after the solder process. The lack of turn-to-turn insulation and the solder in the tape stack allow for highly effective current redistribution around regions of decreased superconductor performance and intrinsically avoid high voltage because the entire coil is a short even at room temperature. The coil has optimized mechanical strength since it is almost all steel, and the solder tape stack was known from cable tests [1] to protect the tapes. Cooling quality is excellent and simple since there is only one pressure boundary, and the Helium has relatively high-conductance paths through the coil.

So, in general, the TFMC [7], [8] confers several advantages including ease of construction and assembly, the absence of high voltages/arcing, and the general ability to adjust to, and be robust to, perturbing events by redistribution of current internally [9]. However, these same features also provide challenges to their use in magnetic confinement, namely that the self-determined nature of the internal current distribution means that the magnetic field amplitude and shape, dictated by the azimuthal current, I_{az}, in the REBCO-filled turns, are not fixed solely by geometry as in a turn-to-turn insulated coil. A particular requirement for SPARC (and generally for tokamaks) is that the azimuthal current/field does not vary by more than 0.5% between the TF coils in order to avoid deleterious TF ripple [6]. This requires that both the superconductor and normal conduction paths be designed and predicted with high precision in order to ensure proper dc coil performance. Furthermore, the ac performance of the coil must be predictable in order to understand the aspect of coil charging (timescales and power and cooling requirements) and robustness to off-normal events. Therefore, a primary objective of the TFMC tests was the validation of numerical modeling tools, to not only interpret the test results but also to project forward to the required performance in SPARC.

A. *Computational Models*

A hierarchical approach was taken in developing computational models for the TFMC with the strategy of trading physics fidelity with computational speed and flexibility. The three models in descending order of fidelity and ascending order of speed are labeled: 1) mBS; 2) nested loop; and 3) circuit model. Short descriptions follow here with detailed descriptions to be covered in forthcoming articles.

The "multithread Biot–Savart" or mBS code has full 3-D fidelity of the coil including the spiraling REBCO tape stacks, pancake geometry including joints, structural materials, and interior cooling channels. As implied by the name, the code features a self-consistent Biot–Savart iterative calculation of the magnetic field produced by the internal current and electric field distribution. The iterative scheme is required because the REBCO critical current depends on the magnetic field local to the REBCO stack, yet the magnetic field depends on the current distributions in the entire coil set. The current distribution is altered by the voltages that appear on the REBCO because these can drive ohmic currents in structural materials due to the lack of insulators. mBS switches between an efficient BS solver, resolved at substack spatial resolution, and finite-element analysis (FEA) redistribution of the currents in the TFMC structures until convergence is reached. The code is used in two modes. The first mode is called "mBS-static," which provides the equilibrium solution for the 3-D current, field, and temperature distributions for given input of bus current and cooling. The second mode "mBS-dynamic" solves the current/field/thermal equilibrium versus time with varying input conditions. Typical runtimes for static mode are ∼8–12 h, while a dynamic run can take days to months depending on the severity of the time derivatives in the simulation.

The nested-loop model exploits symmetry in the coil to achieve faster computational speeds while still capturing key aspect of azimuthal nonuniformity. The model is an FEA-based electromagnetic (EM) + thermal solver for one vertical half of the winding pack (WP) with accurate azimuthal shape (i.e., in the D form of the TFMC) but with nested loops of REBCO

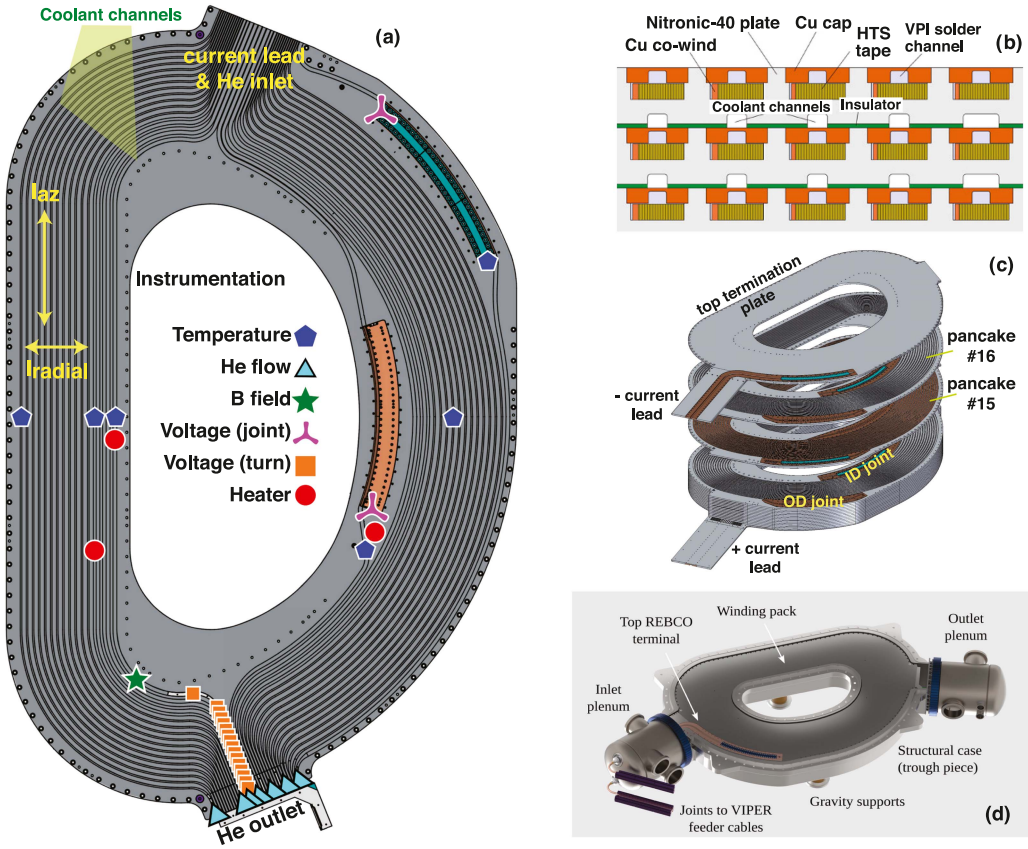

Fig. 1. Schematic of the TFMC. (a) Instrumentation locations overlaid on the cooling channel side of a TFMC pancake plate. Azimuthal and radial current definitions shown. (b) Sample of the WP with orientation of tape stacks on top and coolant channels on bottom. (c) Partially exploded view of the TFMC build showing the tape side of the pancakes, termination plates, joints, and current leads. (d) Assembled TFMC including He plena and current leads.

stacks rather than the actual spirals. No joints are present, so current redistribution among pancakes/turns is inductive. The FEA model resolves the various conductors (copper, REBCO, and structure) and so provides accurate evolution of the local current and heat distribution. This model is particularly useful in following the azimuthally dependent redistribution of currents and field during transient events. A runtime of one week can follow the TFMC all the way into the latter phase of a quench, where almost all the current is being carried in the copper cap/co-wind.

The circuit model treats the REBCO stacks and structural materials as dynamic circuit elements of resistance and inductance. The model can, thus, resolve the current/voltage on a turn-to-turn basis but contains no information about the azimuthal distributions. The model calculates the inductive properties on a turn-to-turn basis from as-built dimensions. The model also solves the thermal evolution of the coil by solving energy balance based on heat capacity and conduction between the circuit elements, representing radial heat transfer in the TFMC. The code is extremely fast, taking several minutes to provide time-resolved evolution of the full 256 turns. The circuit model can be used for predictive modeling of all the aspects of the coil operation (e.g., ohmic power loading and voltages during charging) and to model off-normal events such as bus open-circuit and heating transients.

All three simulation tools use the same REBCO critical current I_c data from tests of the actual tape inserted during pancake assembly. The I_c data include dependence on B amplitude, B-direction (relative to tape plane), and temperature. I_c is extracted from the statistics of the tape tests on every meter of tape inserted into the TFMC and accordingly adjusted to the average number of tapes per unit distance in the assemble stack (see [8] for details). This captures the effects of tape splicing or grading in the REBCO stack. This approach is justified by the excellent current-sharing capabilities of the solder encasing the REBCO tapes in the stack [1]. For the time-dependent simulations, the tape stack was treated as a smeared conductor, which can only partially capture the impact of single tape effects, such as screening currents, while any ac inductive effects are neglected in the static simulations.

B. Measurements

The TFMC featured ~300 internal diagnostics in order to document its performance and validate the EM models. Fig. 1 indicates the measurement locations in the plane of one of the pancakes (see [8] for details). Voltage taps were present on every pancake and across every joint and resolved on a turn-to-turn basis. A small fraction of taps (~15%) became inoperative during cooling and loading but overall pancake voltages could

usually be reconstructed from functioning taps on the same pancake. The turn voltage taps were located on the opposite side of the TFMC from the current bus and joints for ease of implementation and interpretation. Temperature measurements were distributed across the WP volume. Hall probes measured internal B field at the tight-turn corner of the TFMC D, but only functioned in the second campaign.

Measurements external to the TFMC case were also used. Total currents were measured with fiber-optic current sensors [(FOCSs), Condis Electronic Fiber-Optic Current Transformer, HO-2000121)], which feature high accuracy and linearity (see [10] for details of the testing facility and external measurements). The first FOCS was used to measure the bus current entering the TFMC via the current lead. A second FOCS was positioned around the WP to measure the total azimuthal ampere-turns with the average azimuthal current per turn I_{az} dividing this by $N_{turns} = 256$. The FOCS measurement range is up to ~500 kA, so this could only be used to obtain I_{az} up to ~2 kA. Two F71 Lake Shore Cryotronics Teslameters were fixed to the top of the TFMC cryostat to measure the external dipole field to diagnose B fields and, thus, deduce I_{az} at $I_{az} \geq 2$ kA. Strain gauge rosettes were installed on the exterior midplane of the TFMC structural case to measure directional strain.

Data were collected using a combination of MDSplus [11], [12] segmented records and influxDB trends from the programmable logic controller (PLC)-based control system. MDSplus provided programmatic access to the trend data as well as the natively acquired signals, and Grafana, the control system data viewer, had access to the MDSplus recorded signals as well as the influx recorded trends. This allowed the variety of data consumers to access the totality of the measurements using their preferred interfaces. A total of 3.5 TB of data were recorded for the TFMC tests.

C. Test Goals and Description

The goals of the testing are summarized as follows.

1) Confirm basic EM features of the coil such as radial resistance and inductance at resolution of the entire WP, pancake, and turn.
2) Verify the superconducting state of REBCO stacks and quantify their performance compared to original REBCO tape performance and that found in liquid nitrogen pancake tests.
3) Determine the resistance of pancake-to-pancake joints with varying currents, fields, and loads, which can only be measured in an assembled coil.
4) Verify the structural integrity of the TFMC WP and case under varying loads.
5) Understand the dynamic response of the NINT TFMC to transient heating caused by open circuits of bus current.
6) Measure the quench dynamics and resiliency of the TFMC to off-normal events.

TFMC tests were carried out in two campaigns in 2021. The first campaign focused on achieving the SPARC programmatic goal of $B_{stack,max} = 20$T at the REBCO tape stack. The TFMC bus current was ramped to 40.5 kA, $B_{stack,max} \geq 20$T documented over ~3 h, followed by the TFMC being discharged. Fig. 2 summarizes this campaign with the various phases of the test labeled. Following this campaign, the TFMC was returned to room temperature and visual inspections of the TFMC case inside the cryostat indicated no perceivable damage. A second campaign focused on the enhanced interrogation of the REBCO superconductor performance using a fixed bus current of 31.5 kA with slowly varying operating temperatures between 24 and 33 K. This was followed by programmed open-circuit (31.5–0 kA) quench to test the TFMC dynamic response and resiliency. Subsequently, the coil was recooled to $T = 24$ K and electromagnetically tested with bus currents up to 12.5 kA. The TFMC was then discharged, warmed to room temperature, removed from the cryostat, and disassembled for visual inspection.

III. Test Results and Model Comparisons

A. Pancake Tests in Liquid Nitrogen (LN_2)

Modularity is a significant advantage of the REBCO no-insulator TFMC design. A particular advantage is the ability to stress and test the REBCO superconductor in each pancake following the tape insertion and soldering; both the processes can affect the REBCO superconductor. Two key advantages result: first, the ability to optimize placement of pancakes within the WP to maximize performance given as-built test results, and second, the ability to reject pancakes before insertion into the WP that do not meet rigorous acceptance criterion. This information can be achieved in a relatively simple manner by immersing the pancake in a liquid nitrogen LN_2 bath and supplying varied current, featuring the advantage of high-temperature superconductor REBCO over low-temperature superconductors such as Nb_3Sn and NbTi. Measured pancake radial voltages and the azimuthal turn current (using an FOCS) provide data to be compared to the models that use ideal or "pristine" tape I_c to ascertain the changes to I_c produced by the pancake fabrication.

An example of such a test is shown in Fig. 3, where bus current flattops are used to measure the asymptotic response of the pancakes. Comparing I_c and radial voltages to mBS-static model predictions provides a quality fit for an I_c scalar correction factor that captures the relative degradation in the REBCO stack at a pancake level. The causes of this degradation could be physical damage to the REBCO layers during tape insertion and solder, modifications to the REBCO crystals caused by the chemical and thermal environment during soldering, or induced strains on the REBCO layers caused by the heating/cooling cycle during soldering. Azimuthal and radial current versus bus current, REBCO current saturation, and mBS-static runs are used to obtain I_c scalar correction for the pancake. The REBCO tape is purposely pushed to the saturation level, i.e., additional current primarily goes into radial current rather than azimuthally since the critical current is being approached or surpassed. This is a rigorous test of the REBCO performance allowed by the low magnetic energy of a single pancake, which is being operated at relatively low current (~10 kA) and the robust cooling of the pancake in the LN_2 bath. A compilation of pancake REBCO

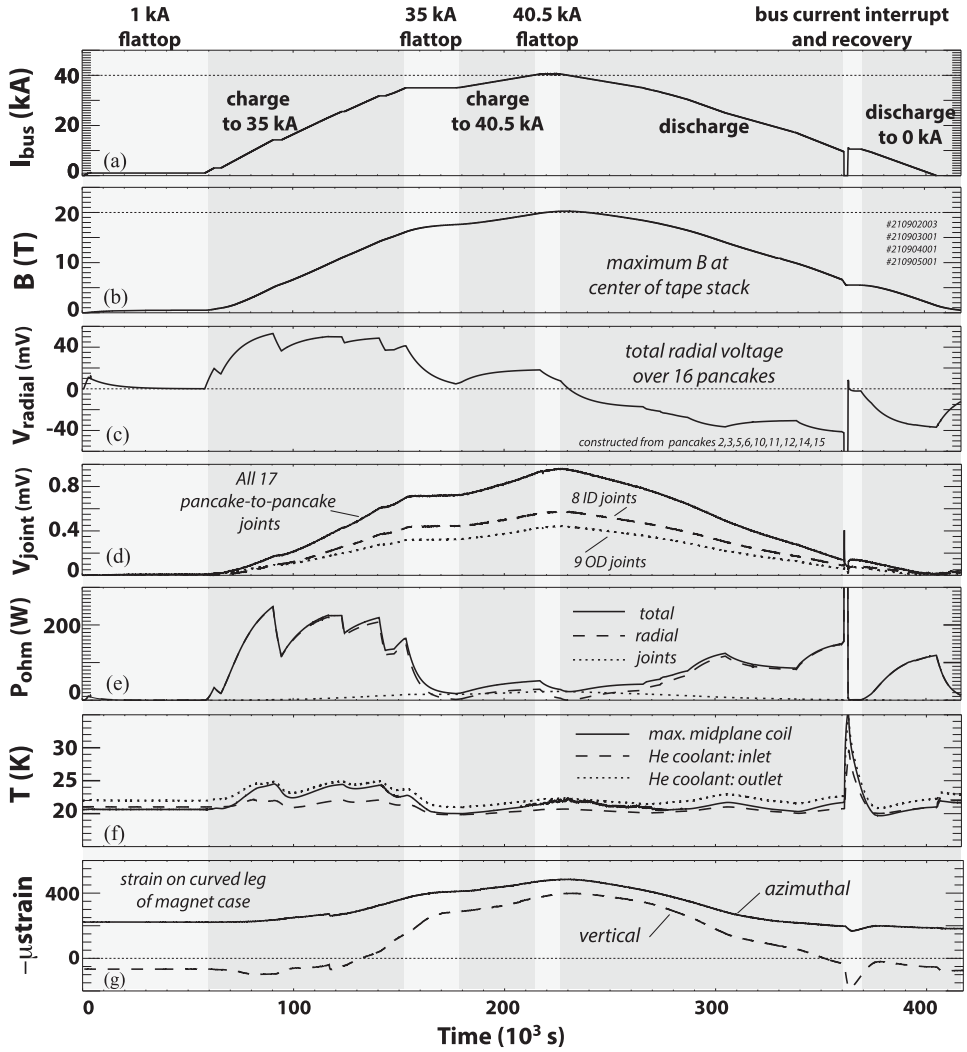

Fig. 2. Summary of TFMC 20-T test. (a) Bus current with different phases of test labeled. (b) Maximum B on REBCO tape stack. (c) Total radial voltage on coil. (d) Total voltages on pancake-to-pancake joints including a breakdown of contributions from OD and ID joints. (e) Ohmic heating power in WP from radial and joint voltages. (f) Temperatures of He coolant inlet and outlet, and the maximum T measured in coil. (g) Microstrain measured on exterior of TFMC structural case in azimuthal (co-current) and vertical directions.

superconductor performance from LN_2 test for all 16 pancakes is shown in Fig. 4(a) and (b). The electric field along the stack follows the standard relationship for REBCO superconductors:

$$E = E_c \left(\frac{I_{az}}{I_c} \right)^{n-\text{value}} \quad (1)$$

where $E_c = 10^{-4}$ V/m is the predefined critical electric field and I_{az} is the azimuthal current providing the ampere-turns in the coil. In the model, n-value is not ascribed from the REBCO tape data and so is determined from the LN_2 test alone. The n-value varies from 17 to 21, indicating good superconductor performance. The I_c scalar corrections vary from 0.96 to 0.985, with no obvious correlation to n-value. These values were used for predictions of the full TFMC performance. The modest decreases in I_c, and high n-values provided confidence in the pancake assembly process and the "as-installed" pancake performance in the full TFMC. The TFMC project placed an administrative limit of rejecting any pancake that had an I_c scalar correction lower than 0.94 since this would lead to approximately doubling the electric field compared to the average pancake stack performance (scalar correction 0.97). However, no pancake was rejected due to this administrative limit.

B. Noncryogenic TFMC WP Tests

Testing the TFMC at room temperature and 100 K at low current confirms the coil's mechanical viability. The joint voltages indicate correct pancake/joint assembly, current continuity, and instrumentation functionality. The measured voltages are quantitatively compared to mBS-static model predictions at both temperatures in Fig. 5.

C. TFMC EM Performance

The first campaign included phases of charging/discharging and current flattops (see Fig. 2) to characterize the EM response

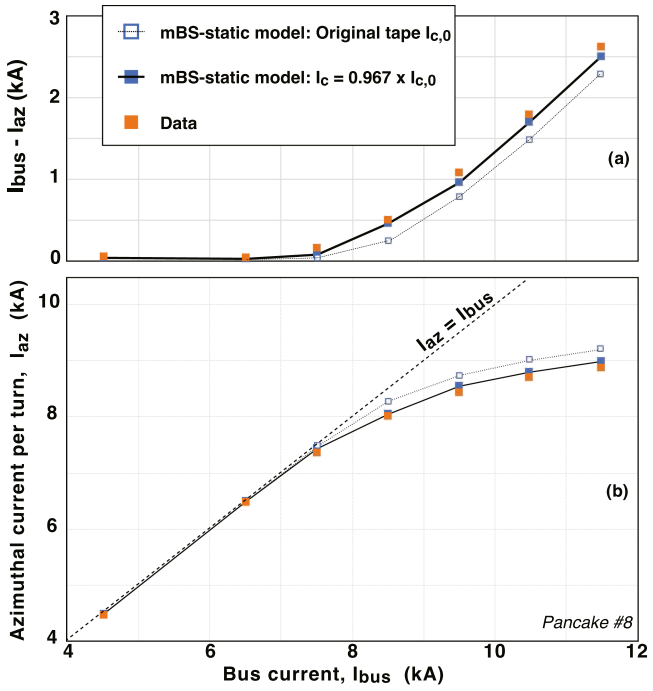

Fig. 3. Example of liquid nitrogen LN_2 pancake characterization of critical current I_c. Data are compared to the mBS-static model predictions using original REBCO tape data and with a fitted scalar correction to I_c of 0.967. (a) Difference between bus current and azimuthal (per turn) current. Current conservation requires this difference to be the turn-to-turn radial current. (b) Azimuthal (per turn) current compared to bus current.

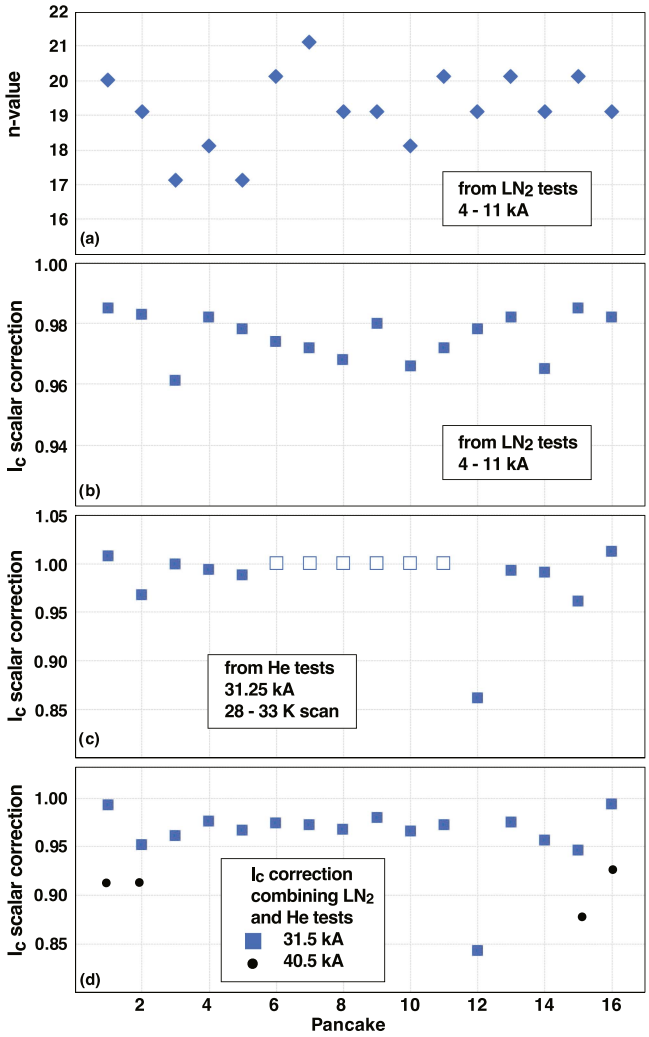

Fig. 4. Summary of pancake superconductor performance from various tests. (a) n-value. (b) Critical current I_C scalar correction from liquid nitrogen LN_2 pancake tests (see Fig. 3). (c) I_C scalar correction from 31.5 kA He-cooled flattop T scan (see Fig. 11). Hollow symbols indicate no correction (scalar factor 1.0) for pancakes with asymptotic voltages below the detection limit. (d) I_C scalar correction from combining results of LN_2 and He-cooled tests (blue) and I_C scalar correction from He-cooled 40.5 kA tests at 20 T (black) where only the outermost pancakes have measurable voltages (see Fig. 10).

of the TFMC. Radial resistance R_r of pancakes was assessed during charge/discharge phases at 20 K; see Fig. 6(a) for results. Resistance was determined with two methods: fitted dV/dI_{bus} in early phases of current ramp from 0 to 1 kA, and by $\Delta V \ / \ \Delta I_{\text{bus}}$ with a fast pulse of 0.2 kA during the 1 kA flattop phase. The uniformity of resistance across pancakes indicates quality assembly since inserted components during assembly (solder and Cu caps) contribute to resistance, and therefore, large voids in the solder or poorly adhered Cu caps would result in increased resistance. Modeled radial resistances (from FEA simulations) are ~10% lower than those measured in LN_2. Radial resistance decreases from 77 to 20 K due to decreases in resistivity of pancake structural materials.

Pancake exponential decay time constants [see Fig. 6(b)] are highly uniform and predicted well by the circuit model, which uses the experimentally determined pancake radial resistances. This confirms that the circuit model is accurately calculating the inductances of the pancakes and that the current paths are as expected in the TFMC WP (i.e., there is not another source of current leaking to ground potential such as the TFMC case).

The 16-h flattop at 1 kA (see Fig. 2) was used to allow the coil to relax to a state with very small residual radial voltages; Fig. 6(b) shows these to be ~5 μV, which is close to the noise floor of the taps ~1 μV. The flattop also provides the ability to accurately determine current distributions. Table II summarizes the fields and current at the end of the 1 kA flattop. The average radial current, flowing through the structural material of the pancakes (see Fig. 1), as determined by the set of FOCS, is

TABLE II
CURRENTS AND FIELDS AT THE END OF 1 KA FLATTOP PHASE

Parameter (unit)	Value (uncertainty)
Bus current I_{bus} (A)	1 015.0 (0.1)
FOCS azimuthal current I_{az} (A/turn)	1 006.5 (0.3)
Average radial current $I_{\text{bus}} - I$az (A)	**8.5 (0.4)**
Average pancake radial voltage, V_r (μV)	6.8 (1)
Average pancake radial resistance, R_r (nΩ)	716.4 (14)
Average pancake radial current, V_r / R_r (A)	**9.5 (1.4)**
B at external teslameter (mT)	80.3 (0.2)
Teslameter I_{az} conversion factor (A/T)	12 534 (25)

8.5 ± 0.4 A or less than 0.1% of azimuthal current. The accurate knowledge of radial resistance (see Fig. 6) allows the conversion of the overall radial voltage to an average radial current of 9.5 ± 1.4 A. Thus, the radial currents agree within measurement uncertainty and allow one to use V_r/R_r to determine radial

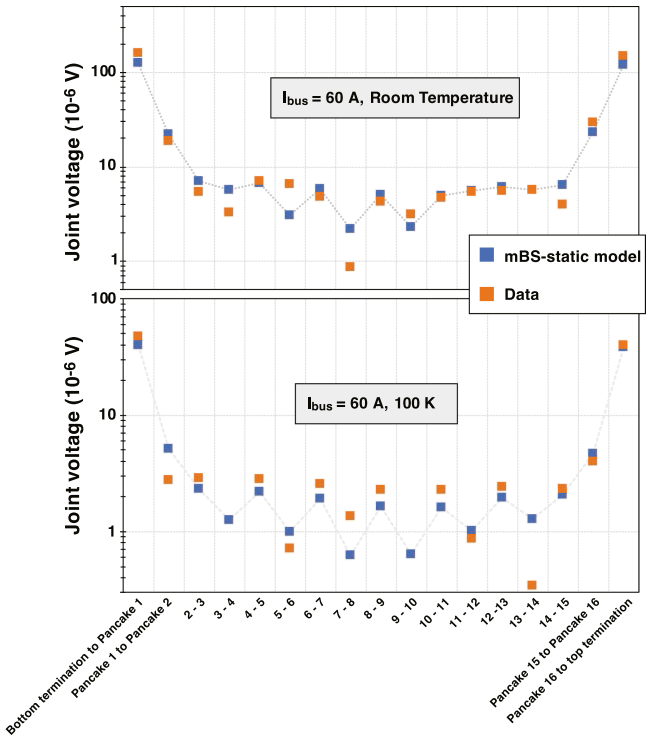

Fig. 5. Room temperature and 100 K continuity and joint testing of TFMC. Steady-state voltages on joints shown from 60-A bus current, comparing data with predictions from the mBS-static model.

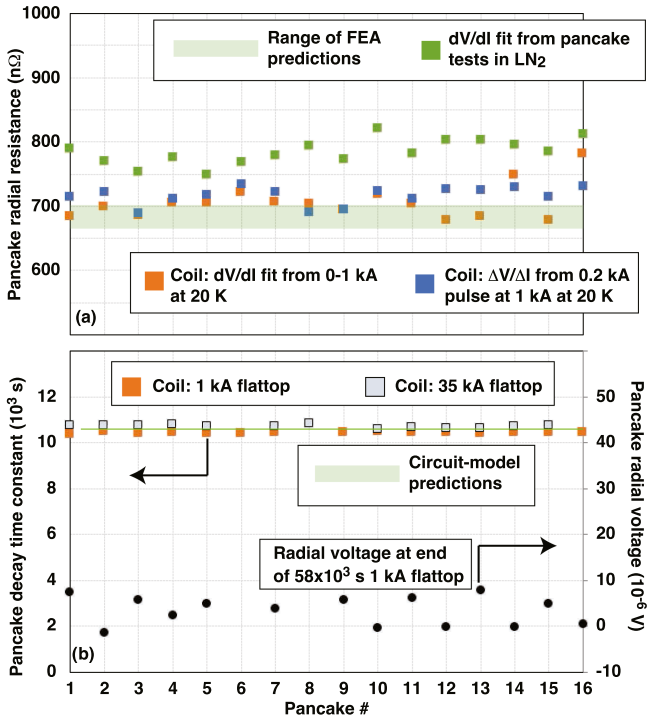

Fig. 6. Pancake resolved EM TFMC properties. (a) Pancake radial resistance. Green symbols and bar show data and FEA model comparisons at 77 K LN_2. Orange and blue symbols obtained at 20 K from current ramp and a 0.2 kA current pulse, respectively. (b) Fitted exponential decay times measured during 1- and 35 kA flattop phases of 20-T test (see Fig. 2) compared to circuit-model predictions. Black circles are fitted asymptotic voltages from 1 kA flattop phase.

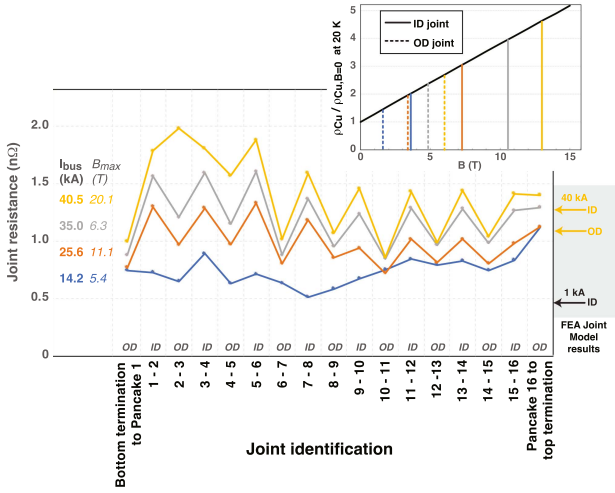

Fig. 7. Joint resistances measured at four flattop bus currents. Location of joint in coil and OD and ID joints are labeled. B fields are obtained from teslameter I_{az} and mBS-static. Top right insert: normalized increase in copper resistivity versus B [13], with estimated B field values at ID and OD joints indicated at each bus current. Bottom right insert: Resistance predictions from the FEA joint model [14] for 1 kA (low B) and 40 kA (high B) cases.

currents in flattops/azimuthal currents outside the measurement range of the I_{az} FOCS. In addition, the external teslameters were cross calibrated to the FOCS to determine the conversion factor between local B field at the teslameters and the azimuthal current.

Several bus current flattops were used on the charging of the TFMC in the first campaign (see Fig. 2). This allowed the operators to assess and control the TFMC heating during the charging and also provided an opportunity to assess the pancake-to-pancake joint resistances, with results shown in Fig. 7. In general, the joint resistance is uniform and low $\sim$1 Ω, below the initial estimates of $\sim$5–10 Ω. As the bus current and B field increase, a clear pattern of increased resistance appears on the inner diameter (ID) joints compared to the outer diameter (OD) joints, along with a general increase in all the joint resistances versus B. This is expected from the magnetoresistance of copper [13], which makes up the majority of the joints. The insert in Fig. 2 shows that the expected relative increase in copper resistivity overlaid with the average B fields at the joint locations is roughly consistent with the measured pattern, i.e., ID joint resistance approximately doubles between the 14.2- and 40.4 kA cases. Subsequent to the TFMC test, a thorough study of REBCO-based contact joints was carried out as part of a Ph.D. [14]. An FEA model was developed and benchmarked to well-diagnosed benchtop joints. The study found that FEA spatial resolution at the micrometer level, similar to the REBCO layer thickness, was required to properly capture the current transfer from the tape to the Cu joint. Applying this model to the TFMC joints (see [14, Sec. 5.4.4]) at low and high B limits yields satisfactory absolute and versus B comparison to the data (right insert of Fig. 7). The Pancake 2 to Pancake 3 joint appears to develop higher resistance at the 40.5 kA step. This may be

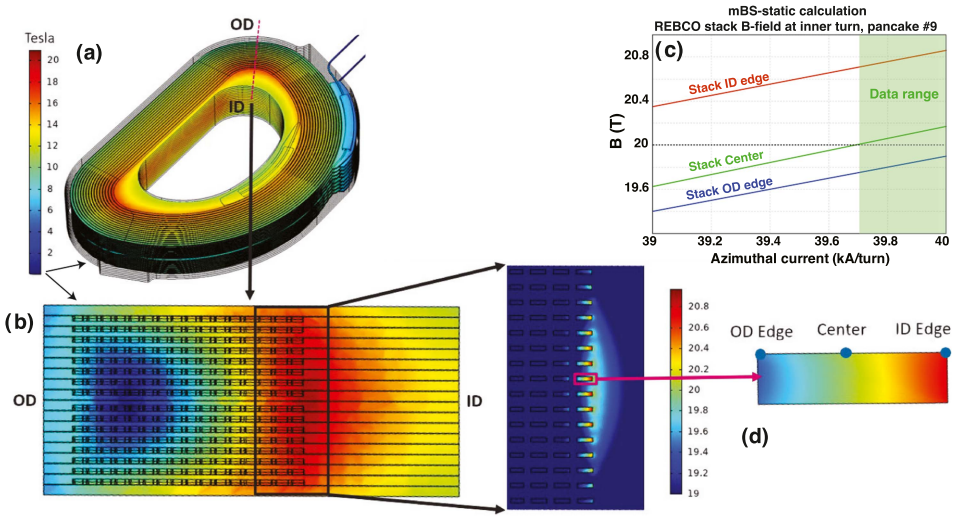

Fig. 8. Magnetic field distributions in TFMC calculated from mBS-static simulation. (a) 3-D rendering of TFMC WP at $I_{az} = 40$ kA. (b) Cross-sectional cut of WP at azimuthal location of maximum B field. (c) Calculated values of B across REBCO tape stack on Pancake #9 inner turn at azimuthal location shown in (b) as function of I_{az}. (d) Magnified cross section of high-field ID turns from (b) with zero-suppressed color scale for viewing clarity.

attributed to a loading effect, but no discernible damage was found on this joint at disassembly.

Fig. 2 summarizes the first campaign test. Radial voltages nearly exactly follow the simulation predictions from the circuit model using the bus current waveform for input (expected since the circuit model uses verified R and L for the coil). The joint voltages vary smoothly with time/current showing no obvious impact from the Lorentz loading of the coil. The joint voltage is seen to follow the magnetic field due to the magnetoresistance of the copper in the joint. The ohmic power inside the WP is dominated by radial voltage until $I_{bus} \sim 35$ kA when the joint dissipation ($\propto I_{bus}^2$) rises to ~30 W. The resistances of the copper–REBCO interfaces in the current leads are 5.2 nΩ ([15]) leading to 8.5 W at 41.5 kA, constituting the other significant helium heat load at flattop. The supercritical He cooling system, with a maximum capacity ~600 W at 20 K [16], readily maintains acceptable coil temperatures < 25 K during the charging and at maximum current.

Structural case strain increases smoothly with increasing B with the exception of a small slip at 120 000 s [see Fig. 2(g)]. The unplanned bus current interrupt at 9 kA is analyzed in Section III-F.

During the ~3-h flattop at I_{bus} 40.5 kA, the maximum B field at the center of REBCO tape stacks exceeded 20 T, meeting the programmatic goal of the test. The B field distribution inside the WP determined from mBS-static Biot–Savart simulations is shown in Fig. 8(b) at the "tight-turn" high-B corner of the TFMC with an azimuthal current of 40.0 kA imposed to assure $I_{az} = I_{bus}$). Large fractions of the inner turns experience B fields near 20 T. The programmatic goal was, more specifically, that the center of a REBCO tape stack exceeded 20 T in conditions representative of the SPARC TF. High-resolution scans of the B field by mBS-static on the innermost turn were used to determine the precise ratio between azimuthal current and the B field at the REBCO stack center. Table III tabulates the result of the azimuthal current and B-field determinations at the peak B field, and the

TABLE III
CURRENTS AND FIELDS: 40.5 KA PHASE

Origin	Parameter (unit)	Value (uncertainty)
Bus FOCS	I_{bus} (A)	40 473 (81)
Teslameter #1	I_{az} (A)	39 690 (79)
Teslameter #1	$B_{stack,max}$ (T)	**20.02 (0.04)**
Teslameter #2	I_{az} (A)	40 708 (81)
Teslameter #2	$B_{stack,max}$ (T)	**20.53 (0.04)**
Voltage taps	Average $V_r(\mu V)$	471.1 (4)
Voltage taps, R_r	Average $I_r = V_r/R_r$ (A)	658 (13)
Taps, R_r, $\nabla j = 0$	$I_{az} = I_{bus} - I_r$ (A)	39 815 (82)
Taps, R_r, $\nabla j = 0$	$B_{stack,max}$ (T)	**20.08 (0.04)**
FOCS + voltage zero crossing	$I_{az} \approx I_{bus}$ (A)	39 930 (80)
FOCS + voltage zero crossing	$B_{stack,max}$ (T)	**20.14 (0.04)**

range of results is shown in Fig. 8(c). All the measurements show $B_{stack,max} > 20$ T outside of experimental uncertainty. The two teslameters did not agree within their stated precision of 0.2%. It is not believed that the teslameters moved during the experiment since no sudden change in B measurements was seen on either teslameter. The teslameters were attached to different structures on the TFMC cryostat, so the present speculation is that they were impacted by the magnetization of nearby components. Current accountancy by the use of voltage measurements, which was validated at low current (see Table II), has close agreement to teslameter #1 result, so we conclude that $B_{stack,max} \approx 20.1$T is the most accurate statement, while the maximum field in the coil certainly surpassed 20.3 T. As the coil was starting to discharge from 40.5 kA, the total radial voltage on the coil crossed zero. While not highly accurate due to the slightly nonuniform internal voltage distribution in the WP, this point provides another estimate of the azimuthal current by assuming that it is simply equal to the bus current. This method yields a similar result of $B_{stack,max} = 20.14$ T.

Example thermal responses of the TFMC during first test campaign are shown in Fig. 9. At the peak bus current and B

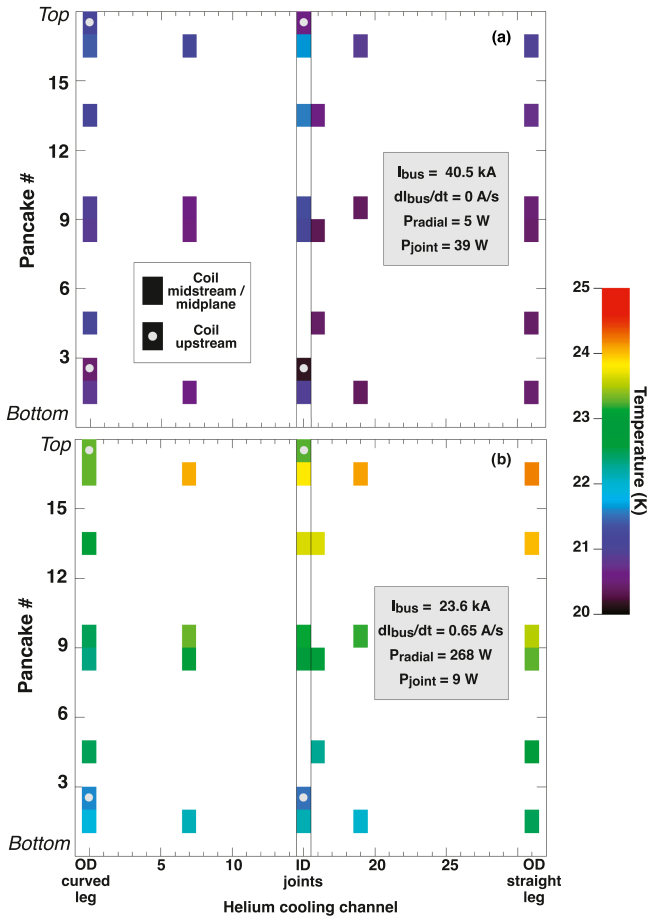

Fig. 9. WP temperature distribution at example times during first campaign test (see Fig. 2(a)) during 40.5 kA flattop phase at time of peak B field (see Table III) and (b) during charging to 35 kA, at the time of peak ohmic heating radial voltage. Color-coded temperatures plotted versus cooling channel (with 16 cooling channels in each leg) and pancake number or locations on the ID joints. Temperature measurements at midplane of coil, i.e., midstream between the He inlet and outlet plena, and upstream locations closer to the He inlet are labeled. Inserts show global coil current and heating parameters.

field, the WP has highly uniform and low temperatures. The dominant heating term is from the joints, but neither the upstream or downstream ends of the joints show significantly higher T. This results in modest total joint heating, 39 W, due to the low resistances of the joints (see Fig. 7). During coil charging, the radial heating is the dominant heat source at 268 W resulting in an equilibrium maximum interior WP temperature $\sim$24 K. The radial (horizontal) temperatures are roughly constant across pancakes, as expected since the radial ohmic heating, arising from radial currents, should be roughly uniform. However, a clear temperature difference of $\sim$2 K is seen from the bottom of the WP to the top. This may be due to buoyancy effects in the He cooling, but this remains an open question for He flow simulations.

D. TFMC REBCO Superconducting DC Performance

The asymptotic voltages at current flattops provide a test of the REBCO superconductor stack performance at high B when compared to the models using original tape data and pancake I_c scalar correction factors from the LN_2 tests (see Section III-A). This methodology is a significant extrapolation in REBCO performance with factors up to 4 in current density and temperature and factors up to 20 in magnetic field. This extrapolation makes the comparison also a test of the simulations. Fig. 10 shows the comparison between mBS-static and the circuit model in determining the turn-resolved voltage distribution at $I_{bus} = 40.5$ kA on the outermost pancakes, which was the only region in the TFMC with measurable voltages. Both the models use the same I_c scalar correction factors tabulated in Fig. 4(d). Experimental data obtained from fits of the voltage decays are compared to the models. The asymptotic voltage could be accurately obtained by fixing the L/R decay times on each pancake to their known values from low current phases (see Fig. 6). Agreement is seen between both the models and the data, despite the large differences in physics fidelity between the models. The measured voltage pattern arises from the decrease in I_c at the top and bottom middle turns of the outer pancakes since this is where the dipole field turns to be largely perpendicular to the tape surface (this effect will not occur in a set of TF coils). The agreement in the patterns of voltages provides further assurance that the current distribution in the coil is dominated by azimuthal current along the REBCO stacks, with small "leakage" radial current determined by the small voltage arising on the REBCO; otherwise, the simplified circuit-model current paths would differ from mBS and the data. Based on these voltages, the average asymptotic radial current on four outer pancakes is 330 A, and nearly zero on the other 12, implying a global azimuthal current "deficit" of $\sim$82 A, or $\sim$0.02%. This meets another programmatic goal of establishing means to have an azimuthal current deficit of $<$0.5% to ensure acceptable TF ripple losses in SPARC. It is noted that the absolute voltage levels required a $\sim$10% correction to I_c compared to the LN_2 results.

The second campaign provided additional tests of the TFMC REBCO performance. The bus current was fixed at 31.5 kA (the operational current of the TF in SPARC), and the coil was allowed to relax inductively at fixed $T = 24$ K for 65 000 s, or approximately six e-folding L/R relaxation times. This allowed accurate measurements of the "residual" voltage on the pancakes [see Fig. 11(a)], i.e., voltages not due to inductive charging effects but from linear resistances in the REBCO stack from local I_c dropouts and current redistribution. Such linear resistances are seen in the test of linear samples of REBCO tape stacks but are more difficult to identify in short-duration coil tests due to inductive voltages. The data, open symbols in Fig. 11(a), exhibit a scatter pattern of voltages across the pancakes with average value of 6.5 μV. There are two reasons to attribute this to "residual" linear resistance. First, this pattern is unlike the voltages that should appear from REBCO superconductor voltages following (1), which should maximize at the top and bottom pancakes due to the field magnitude and directions perpendicular to tape surfaces [see Fig. 11(b)–(d)]. Second, the voltages significantly exceed the mBS-static model, that does not include residual resistance, voltage predictions that are mostly below the detection threshold of 1 μV. These low voltages are expected because I_c is relatively high at this low $T = 24$ K and intermediate B. This observation provides the minimum radial "leakage" current possible in the TFMC as

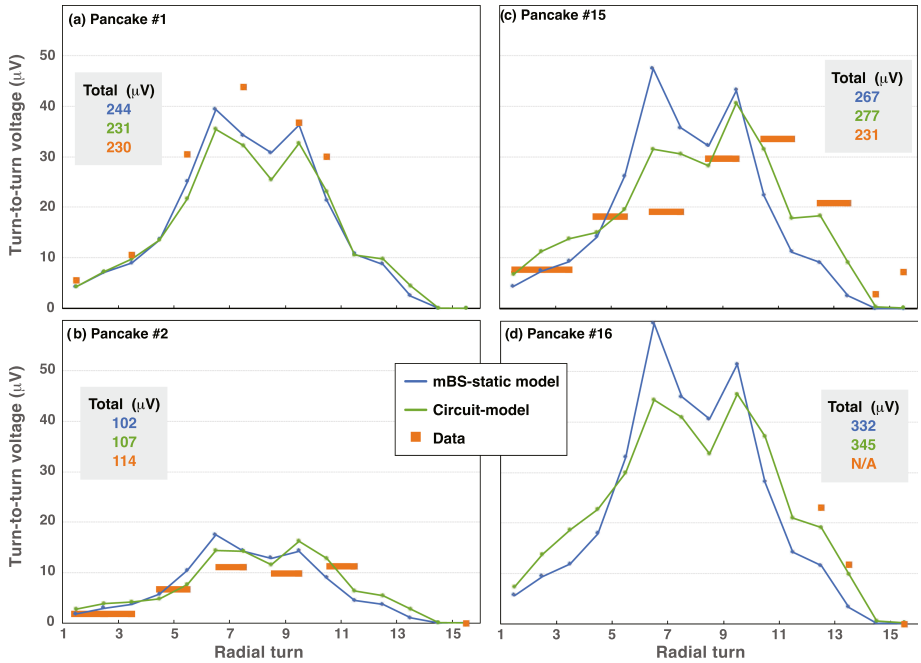

Fig. 10. Voltage distributions on outer pancakes at $I_{bus} = 40.5$ kA and $B_{peak} > 20$ T. Data represent fitted asymptotic dc voltages, compared to electrostatic models at $I_{az} = 40.5$ kA from mBS-static (blue line) and circuit model (green line). Models use I_c scalar corrections factors shown in Fig. 4(d). Data horizontal bars indicate average turn-to-turn voltage where voltage taps span more than one turn. Data are shown where valid voltage tap data exist. Insert tables: total radial voltage from models and data color-coded to match plotted symbols. (a) Pancake #1. (b) Pancake #2. (c) Pancake #15. (d) Pancake #16.

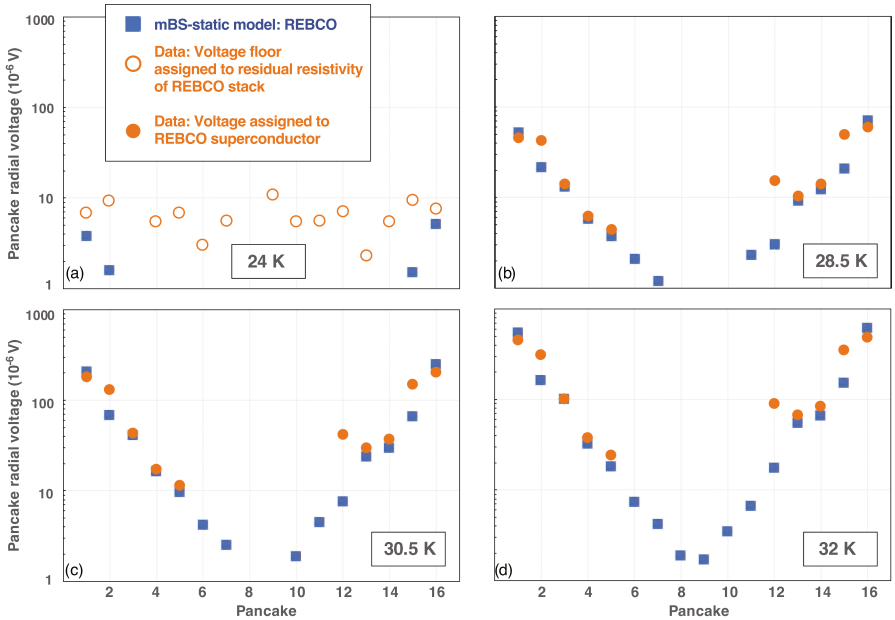

Fig. 11. Pancake asymptotic voltage distributions versus TFMC coil temperature at $I_{bus} = 31.5$ kA at (a) 24 K, (b) 28.5 K, (c) 30.5 K, (d) 32 K. Open symbols in (a) are assigned to "residual" resistivity from I_c dropouts in REBCO stack. Closed symbols (orange) are fitted asymptotic voltages versus time with residual voltages subtracted and are assigned to varying REBCO I_c. Prediction from mBS-static model of voltages due to REBCO I_c variation shown in blue.

being 6.5 μV/R$_r$ = 9.1A at 31.5 kA and $T = 24$ K, or 0.03% of the azimuthal turn current. Since this is the operating current for the TF in SPARC and is at higher operating temperature, we can conclude that the residual resistance in the soldered REBCO should not introduce significant variability in B from coil to coil. Furthermore, we can use the REBCO stack geometry (length ~88 m per pancake, average cross-sectional area ~46 mm^2) and the bus current to estimate a residual resistivity $\rho \approx 10^{-16}\,\Omega\cdot$m. Simulating this residual resistance in REBCO tape stacks will be the subject of future studies.

Following on from the "fully relaxed" coil at 31.5 kA at $T = 24$ K, the operating temperature was increased in incremental steps to flattop values of 28.5, 30.5, and 32 K in order to assess the REBCO superconductor performance versus

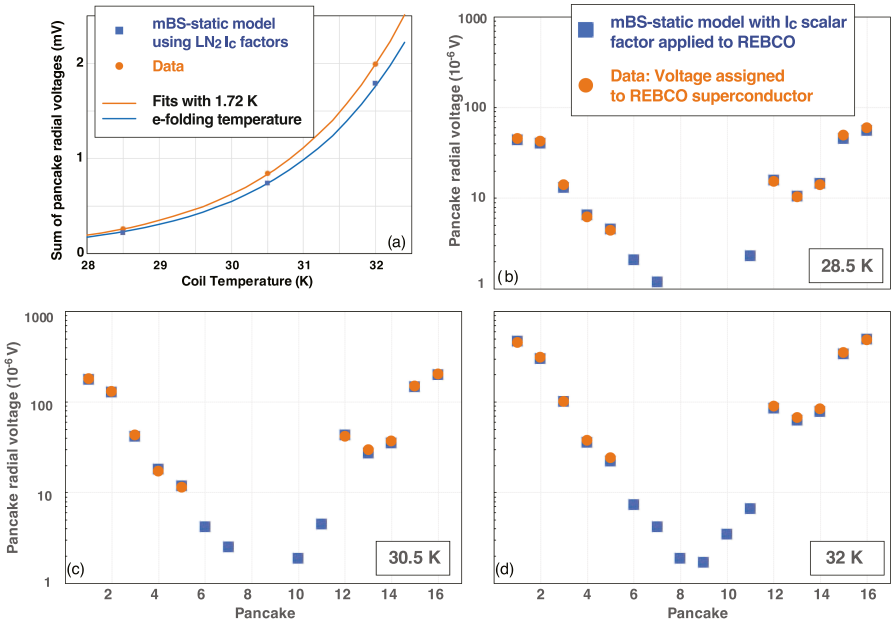

Fig. 12. Pancake asymptotic voltage distributions versus TFMC coil temperature at $I_{bus} = 31.5$ kA. (a) Total coil radial voltage as a function of operating temperature. Symbols are data and mBS-static model using $LN_2 I_c$ factors [see Fig. 4(b)]. Lines are fits to data and model with $T_f = 1.72$ K e-folding temperature $V \propto \exp(T/T_f)$. Pancake asymptotic voltages at (b) 28.5 K, (c) 30.5 K, and (d) 32 K. The mBS-static model uses an I_c scalar factor applied to each pancake, shown in Fig. 4(c) and (d), combining the correction from both LN_2 and He 31.5 kA (see Fig. 11) tests.

T. At each T flattop, the coil voltage was allowed to relax to steady state. The pancake-resolved voltages are shown in Fig. 11(b)–(d), where the "residual" voltages of Fig. 11(a) have been subtracted from the measured voltages. Therefore, the data (orange circles) are ascribed to REBCO superconductor voltages due to varying critical current I_c via (1). These are compared to mBS-static predictions for REBCO superconductor voltages using I_c from LN_2 test [see Fig. 4(b)]. There is generally good agreement between the data and the simulation, both in magnitude and pattern of the voltage. One exception is Pancake #12, where the voltage is higher than the prediction, and also clearly stands out as not following the experimental pattern, being $\sim 3\times$ higher than its mirrored Pancake #5. Pancake #12 is exceptional in the TFMC design in that it was the only pancake of those situated in the bottom (or top) five pancakes that had a low grading of REBCO tape performance with $B = 20$ T, $T = 20$ K projected average $I_c = 682$ A/mm^2, in comparison to $B = 20$ T, $T = 20$ K projected average $I_c = 786$ A/mm^2 in the other nine outer pancakes. This observation of a break in up-down symmetry will be important for the open-circuit quench (see Section III-G). The second exception is the data-to-model mismatch on Pancakes #2 and #15. In this case, the model and data are up-down symmetric, but the model consistently underpredicts the voltage by a factor of 2. These two exceptions indicate that there are limitations in accuracy at pancake-to-pancake resolution in only using data and I_c correction extrapolated only from the LN_2 tests. Nonetheless, these extrapolations suffice at a global level, as shown in Fig. 12(a), which summarizes the data to mBS-static comparisons for the overall radial voltage on the coil. Both the simulation and the data follow the same exponential dependence $V_r \propto \exp(T/T_f)$ where $T_f = 1.72$K is the e-folding temperature. The absolute voltages are within $\sim 15\%$. As with the 40.5 kA case, this directly demonstrates the effectiveness of using the I_c scalar corrections from the LN_2 tests to predict the TFMC performance at low T and high B, despite the large extrapolation in the absolute values of I_c. This also confirms the fidelity of the B and T dependencies on I_c from the REBCO tape tests.

The models can be further refined for their voltage predictions by allowing a second I_c scalar correction to be applied on each pancake. The result of this exercise is shown in Fig. 12(b)–(d), with the second I_c scalar corrections shown in Fig. 4(c). The data to model agreement becomes excellent across the different T with application of this second scalar. It is interesting to note from Fig. 4(c) that the second scalar values generally scatter around unity, indicating that we are likely at the resolution limit for the extrapolations from $T = 77$ K, low-B to T $\sim$ 30K, high-B. As previously noted, the clear exception is Pancake #12, which shows a $\sim 14\%$ "degradation." The precise causes of this outlier remain unclear since postquench examinations of the REBCO stack in the nondamaged parts of Pancake #12 had no obvious flaws and Pancake #12 had LN_2 performance within the distribution of the other pancakes (see Fig. 4). We surmise that some combination of the designed lower high-B I_c value on Pancake #12 and difficulties in the accuracy of the extrapolation of the LN_2 result are the root causes, but this remains an active area of investigation as further NINT coils are being constructed. Fig. 4(d) shows the final I_c scalar corrections used in the codes from multiplying the factors from the LN_2 and He tests. With the exception of Pancake #12, the factors are within 5% of the ideal.

E. TFMC Structural Response

The TFMC structural response was monitored by measuring strain on the midplane exterior of the case. The time dependence of the azimuthal (co-current) and vertical strain are shown in

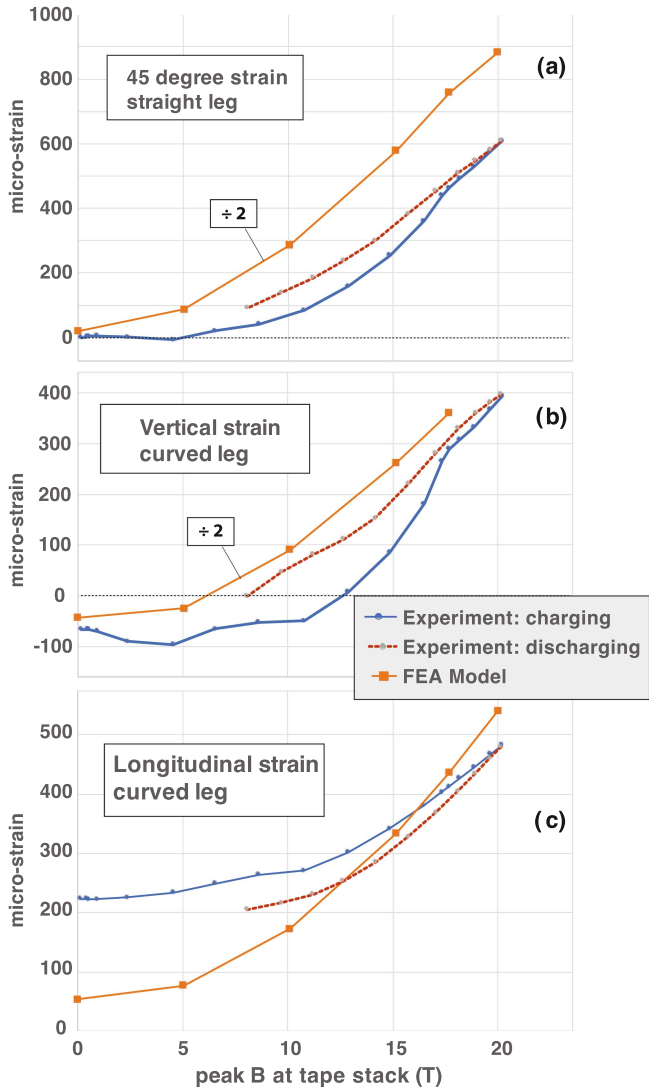

Fig. 13. Microstrain measurements from the midplane exterior of the TFMC support case versus $B_{max,stack}$ for all functioning strain gauges during first TFMC test campaign (see Fig. 2). The charge (loading) and discharge (unloading) of coil are plotted separately. Simulated FEA static loading strain results at six different I_{az}/B values are plotted for comparison. Longitudinal refers to direction parallel to coil current (horizontal in the lab). (a) Strain on TFMC straight at 45° between longitudinal and vertical. Model results divided by 2. (b) Vertical strain on the curved leg. Model results divided by 2. (c) Longitudinal strain on curved leg.

Fig. 2(g) from the first test campaign with no evidence of major slips during loading and unloading. An FEA model of the TFMC WP and structural case was used to predict stress and strain at fixed azimuthal currents (which sets the B field and Lorentz loading). The predicted stresses are considerable, with a peak von Mises stress $\sim$ 900 MPa inside the WP at $I_{az} = 40$ kA. The model predictions for case strain are compared to the viable strain measurements in Fig. 13 as a function of peak B field at tape stack. The data and models see roughly a B^2 dependence. The measured strains vary smoothly versus B for both charging (loading) and discharging (unloading) phases. The model and data also agree on relative trends such as the straight leg experiencing more stress/strain than the curved leg. However, the measured vertical strains are smaller than the model by a factor of approximately 2. It is presently speculated that this is due to the limited ability of the WP to pull the case inward (since the WP wants to compress vertically), and if vertical gaps between the WP case appear, this will lead to smaller than modeled vertical contraction, which assumes uniform contact. The conclusion is that the TFMC structural response to the large Lorentz loading (see Table I) was satisfactory based on the strain measurements. This is self-consistent with the observation that the EM properties like joint resistance, which would be sensitive to internal pancake slips, showed no signs of sudden changes in the campaign (see Fig. 2).

F. TFMC Response to Current Open Circuits

Bus current open circuits are the most concerning transient events for a noninsulated coil like the TFMC. The open-circuit forces the current to internally circulate in the pancakes to satisfy current conservation. So, while the coil avoids high voltages (and arcing), the circulating currents will ohmically heat the coil and raise the temperature, and if this T increase cannot be sufficiently limited, the superconductors and the coil will quench. The TFMC experienced two open-circuit events: one at 9 kA and one at 31.5 kA, which are now described.

An unplanned bus current interrupt open circuit occurred during the discharge of the TFMC from 40.5 kA (see Fig. 2). This occurred due to disruption in external electrical service to the PSFC test facility. The TFMC response is summarized in Fig. 14. The open-circuit occurred at $I_{bus} \sim 9$ kA and $I_{az/}$turn $\sim$12.5 kA. The open-circuit duration was approximately 35 min before control of the power supply was reestablished and the terminal current was reapplied to the TFMC. Pancake radial voltages (summed across turn voltages shown in Fig. 1) immediately arise, with the voltage sign depending on the direction of current in the pancake's spiral, leading to equal but opposite voltage polarities on adjacent pancakes. The radial voltage can be interpreted as a radial current using the known radial resistance of the pancake and is equal to the azimuthal turn current [see Fig. 14(b)] due to the open-circuit requirement for this current to return radially on each pancake. The total voltage across the coil is $\sim$0.16 V, showing the advantage of a no-insulation coil in avoiding arcs. Current is no longer exchanged between pancakes, as seen in the zeroing of the OD joint voltages (the ID joint voltages have an inductive component). This large radial current leads to volumetric ohmic heating of the entire pancake $P_{radial,pancake} = R_r I_{az}^2 = {V_r}^2/R_r$ where R_r is the radial resistance of the pancake $\sim$720 nΩ (see Fig. 6). The cumulative P_{radial} for all 16 pancakes shown in Fig. 14(d) peaks at 2 kW and decreases as the ohmic dissipation decreases the azimuthal current and thus the magnetic stored energy of the coil, since no power is being supplied to the WP during the open circuit. The measured stored magnetic energy decrease of 2.9 MJ during the open circuit agrees with the integrated radial power. The coil temperature has a secular increase as a result of the ohmic heating surpassing the He cooling capacity of 600 W at $\sim$20 K. The rate of temperature increase slows due to three effects: the ohmic heating decreases as azimuthal current decays, the increased

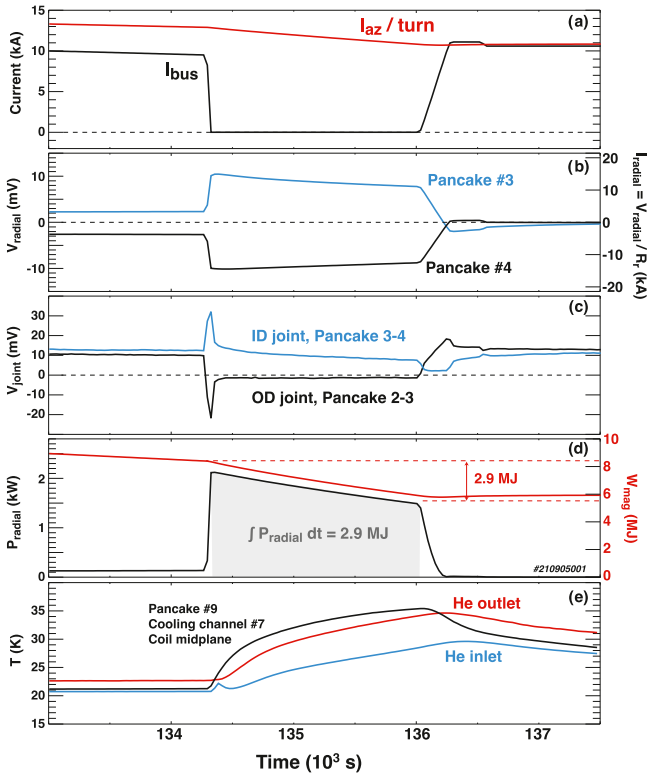

Fig. 14. Summary of unplanned bus current interrupt and recovery phase during discharge of first test campaign (see Fig. 2). (a) Bus current and azimuthal/turn current from Teslameter #1. (b) Example pancake radial voltages on adjacent pancakes and inferred radial currents. (c) Example joint voltages on ID and OD joint in and out of pancake #3. (d) Total ohmic power $P_{radial} = V_{radial}{}^2/R_r$ in 16 pancakes resulting from radial voltage. Magnetic stored energy from azimuthal current and coil inductance (red), compared to the integrated ohmic heating energy of 2.9 MJ. (e) Temperature evolution of He coolant inlet and outlet, and a midplane cooling channel in the curved leg of pancake #9 (see Fig. 15).

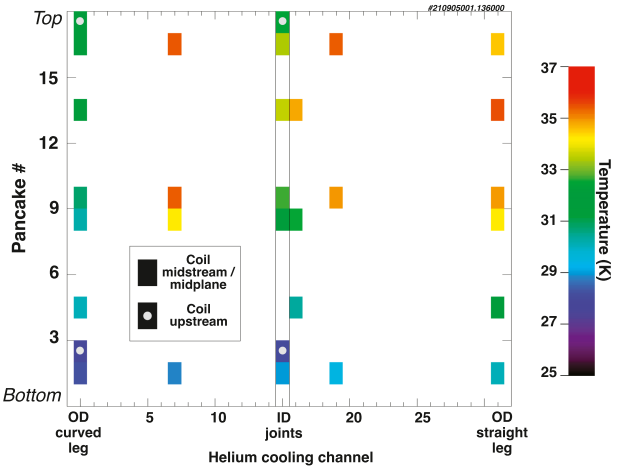

Fig. 15. WP temperature distribution at end of the 9 kA bus current interrupt phase ($\mathrm{time} = 136 \times 10^3$s; see Fig. 14). Color-coded temperatures plotted versus cooling channel (with 16 cooling channels in each leg) and pancake number or locations on the ID joints. Temperature measurements at midplane of coil, midstream between the He inlet and outlet plena, and upstream locations closer to the He inlet are labeled.

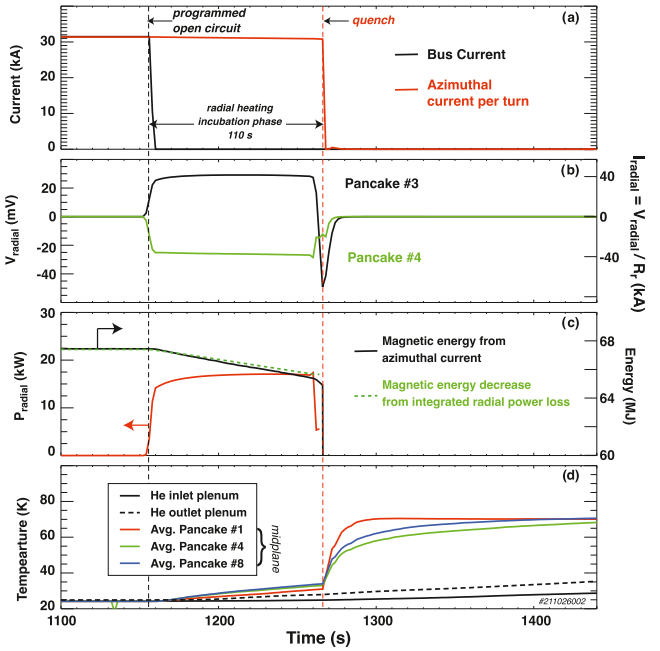

Fig. 16. Summary of 31.5 kA open-circuit quench test. (a) Bus current with programmed open-circuit radial heating incubation phase of 110-s duration leading to the quench of the magnetic field indicated by azimuthal turn current. (b) Sample radial voltages on adjacent pancakes #3 and #4 and inferred radial current. (c) Total ohmic power $P_{radial} = V_{radial}{}^2/R_r$ in 16 pancakes resulting from radial voltage. Magnetic stored energy from azimuthal current and coil inductance (black) compared to the calculated decrease in magnetic energy from ohmic dissipation of P_{radial} (green dashed line). (d) Helium inlet and outlet temperatures, and average midplane temperatures from three sample pancakes in the WP. The He flow was intentionally turned OFF in the time period shown.

He coolant temperature increases its cooling capacity, and the heat capacity of the WP increases as T increases. The highest achieved T of 35 K was insufficient to quench the REBCO superconductors, primarily because I_c is so high at this modest B field (peak $B \sim$6 T). The internal WP temperature distribution at the end of the 9 kA open circuit is shown in Fig. 15. During coil charging (see Fig. 9), there is a noticeable T increase from bottom to top. The peak temperatures are reached in the center of the pancakes, while the joint regions are relatively colder, consistent with radial heating being very high ($\sim$2 kW), while the joint heating/current minimizes during the open circuit. The straight leg has generally higher T.

A programmed open circuit at 31.5 kA and 24 K was used to test the TFMC quench dynamics (see Section III-G). The open-circuit response is summarized in Fig. 16. This has the same features as the 9 kA open circuit except for the increased amplitude of the ohmic heating $\propto I_{az}{}^2$. The radial voltages arise to close the current on each pancake, resulting in $\sim$15 kW of ohmic heating. A modest fraction $\sim$ 4% of the magnetic energy is dissipated by the ohmic heating in this 110-s radial heating incubation phase of the quench. The He coolant circulation was intentionally terminated (although this far surpassed the 0.6-kW cooling capacity) and the coil T rapidly increases in the incubation period, eventually initiating a rapid quench of the azimuthal current/B field. Sample temperatures at the coil midplane increase to 70 K in the 100 s following the quench.

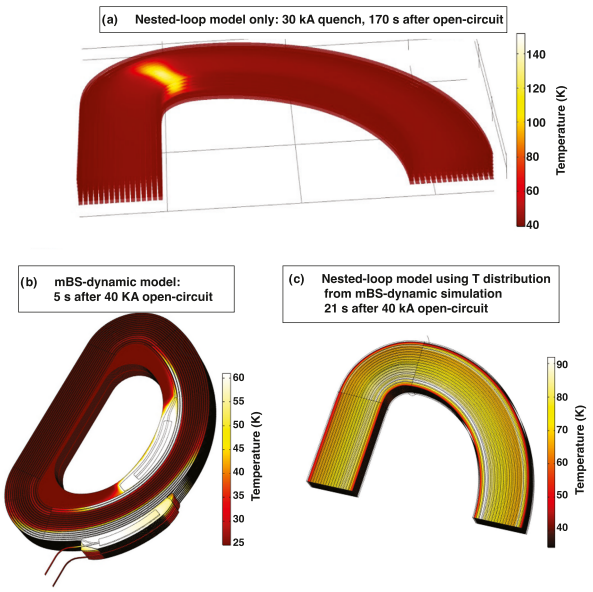

Fig. 17. Example simulations of open-circuit quench dynamics. (a) Nested-loop half-coil model 170 s following a 30 kA open circuit. The appearance of a "radial cut" hot spot is evident in the high-B tight turn corner of the WP. (b) mBS-dynamic FEA model 5 s following a 40 kA open circuit showing hot spots in vicinity of the joints. (c) Nested-loop model results using the (b) result as the starting T distribution and evolving to 21 s after the open circuit, showing a uniform T distribution in the quenched coil with no radial cut.

G. Assessment of Triggered TFMC Quench

The purpose of the programmed open-circuit test (see Fig. 16) was to determine the dominant quench dynamics in a large-scale no-insulation coil like the TFMC and, by extension, the SPARC TF coils. The simulation tools, which clearly perform very well in terms of predicting TFMC dc performance (e.g., Fig. 11), had not converged to a consistent scenario for the quench. An example of this nonconvergence is shown in Fig. 17. Due to its computational speed, the nested-loop model could be used on its own to run from an open circuit all the way through to the azimuthal current being mostly carried in the copper caps and rapidly dissipating the magnetic energy. Fig. 17(a) shows the half-section of the WP 170 s after a 30 kA open circuit. The WP has evolved a hot spot in the tight-turn high-B corner of the coil (see Fig. 8) at a $T \sim 140$ K, far past the REBCO critical T, while the rest of the WP remains near 40 K. The origin of the hot spot is that the starting I_c is lower at this corner due to the high B, forcing the REBCO to push through the critical surface first at the corner. The current shifts locally into the copper cap, which heats the copper, increasing its resistivity and thus cycling up in local heating at fixed current, enforced by current continuity. As the azimuthal current starts to push radially across to avoid the hot spot, it subsequently heats the adjacent turn at the corner. This progresses from turn to turn producing a "radial cut" of the superconductor state, which further concentrates ohmic heating in the corner. This trend continues all the way into the current-in-copper phase of the coil resulting in a large fraction of the magnetic energy dissipated in a relatively small volume, obviously an undesirable outcome. In contrast, the mBS-dynamic model can produce a significantly different outcome. The mBS model is first used to evolve the current and T distribution caused by the open circuit [see Fig. 17(b)] to the point where the peak temperature is 60 K. The ID and OD joints, and the nearby REBCO, are the "hot spots" in this case, caused by the radial current in the pancakes. As the coil gets hotter, the mBS-dynamic simulation becomes extremely slow due to the large T and I_c gradients (attempts at simulation through to the current-in-copper phase were taking more than months). Therefore, the temperature distribution on the WP is used as the starting point for the nested-loop model with the evolved T distribution 16 s later shown in Fig. 17(c). The T distribution is fairly uniform at $\sim$70 K, indicating that the REBCO has mostly quenched and started to current share with the copper. This simulation resulted in peak T, which were less than room temperature.

The quench simulations were run with different parameters, but it remained unclear which result was accurate. On the one hand, the tight-turn "radial-cut" hot spot seemed a robust result originating in the nonuniform I/I_c and the T-dependent properties of copper. Yet, the nested-loop model, by design, lacks important details of the TFMC such as accurate return-current patterns during open circuit and joints, and it was clear that certain T distributions could avoid the radial cut hot spot. Thus, it was determined that the answer must be obtained experimentally with the 31.5 kA open-circuit test (see Fig. 16). Not only would this answer key questions about the overall quench dynamics, but also provide tests of other aspects of the quench such as incubation phase and the impact of transient Lorentz loading on REBCO tape stacks during the quench.

The circuit model was used to scope these issues, with an example open-circuit + quench simulations shown in Fig. 18. The WP voltage and predicted incubation phase of 105 s are in good agreement with the experimental open-circuit response (see Fig. 16). During the quench, the azimuthal turn currents rapidly evolve with middle pancakes "unzipping" their current distributions in under a second. This is caused by rapid inductive coupling of the overcurrents from turn to turn on a pancake, creating a kind of inductive wave that rapidly quenches the pancake [17]. The model shows that the adjacent pancakes get inductively driven and the quench propagates into the phase where the current becomes uniform again [$t = 2.8$ s in Fig. 18(f)] after which the coil's 66 MJ of magnetic energy dissipates in about 1 s, heating the WP to a maximum T of 148 K (recall the circuit model has no azimuthal dependence and so radial cuts are not a possible outcome). The circuit model was used to choose the bus current of the open-circuit quench test since it was determined that the Lorentz loading and in particular out-of-groove forces on the REBCO tape stacks were a good match to those expected in a TF quench event in SPARC. In addition, 31.5 kA gives approximately the same local current density as will be used in the SPARC TF.

The experimental quench EM dynamics are summarized in Fig. 19. Unfortunately, the gains of the voltage taps were incorrectly adjusted, and the turn-to-turn voltages saturated through the quench. Nonetheless, the starting quench dynamics of the turn currents, deduced from the voltages, can be graphically presented [see Fig. 19(c)] for comparison to the circuit model.

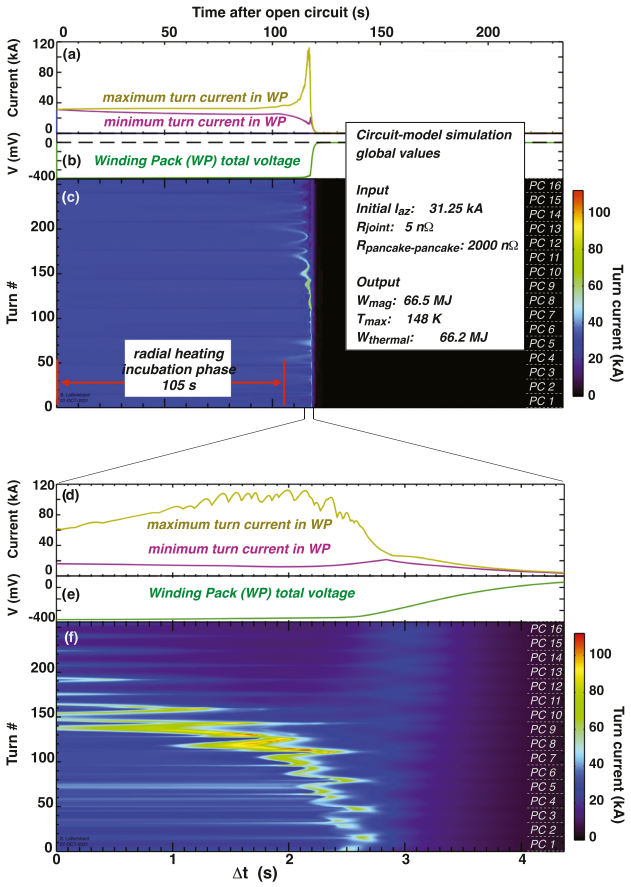

Fig. 18. Circuit-model simulation of 31.5 kA open-circuit quench with top panels showing 105-s incubation phase, and bottom panels magnifying the quench phase of ∼4 s duration. (a) and (d) Maximum and minimum turn current in WP. (b) and (e) WP total radial voltage. (c) and (f) Color-coded turn currents plotted across all 256 turns in the WP with Turn #1 located in pancake #1. Pancake locations labeled as PC # on the right-hand side of the panel.

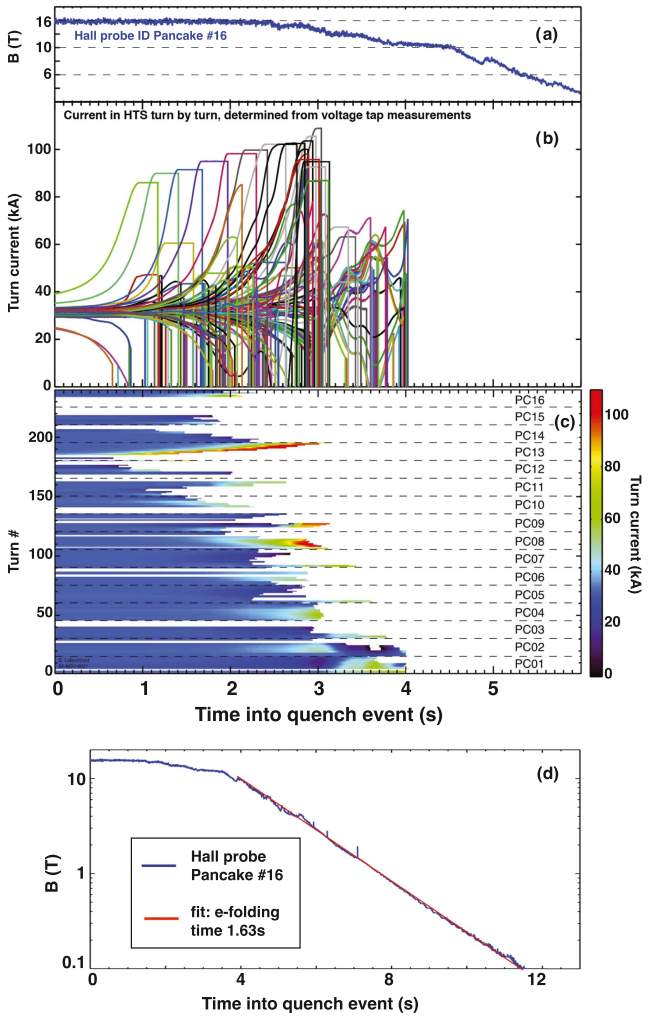

Fig. 19. EM evolution of the 31.5 kA quench. (a) Magnetic field at ID measured with fast Hall probe. (b) Turn currents determined from voltage tap. The flat parts of the traces indicate saturated voltage measurements following which the implied current is forced to zero. (c) Color-coded turn currents from (b) plotted across the 256 turns in the WP with Turn #1 located in pancake #1. Pancake locations labeled as PC # on the right-hand side of the panel. White color indicates the truncation of the turn current plotting due to voltage saturation. See Fig. 18(f) for model equivalent. (d) Logarithm plot of the ID B field from (a) with an overlaid exponential decay fit. Note the expanded timescale compared to other panels.

The rapid turn current inductive "unzipping" on pancakes is seen, particularly early on Pancakes #12 and #13. Peak turn currents are also similar ∼100 kA, and the overall duration of the current redistribution is similar ∼3 s. The current distribution in the copper-current phase of the quench was not measurable due to the V signal saturation, but agreement can be inferred from the similar timescales for the B-field decay. A difference is seen with respect to the first pancake to start quenching: the simulation predicts Pancake #10, while the data show that this occurs on Pancake #12. Recall that Pancake #12 exhibited lower effective I_c, as discussed in Section III-D.

The thermal response to the 31.5 kA quench is summarized in Fig. 20. The T distribution immediately following the quench shows an average temperature ∼70 K with a few locations in the center of the curved leg being somewhat higher. This average T is substantially below that predicted by the circuit model $T = 140$ K due to the ohmic dissipation. This indicated nonuniform magnetic energy dissipation in the WP, with Fig. 20(c) providing an estimate that ∼25% of the magnetic energy was dissipated uniformly in the WP. Following the restart of the He coolant circulation, it was found that the He outlet increased to $T \sim 110$ K. This required that a point between the midplane and the He exit must be hotter than 110 K.

The TFMC was recooled to 24 K. Fig. 21 summarizes the postquench EM test of the TFMC using bus currents ramps and flattops. The current paths for the coil had clearly been altered. The azimuthal current and B are at approximately half the bus current, indicating the loss of effective turns in the coil. The pancake voltages were substantially different. Pancake #4 showed the expected inductive voltage and decay at flattop. Pancake #9 was similar to Pancake #4 at low current but develops a large dc voltage at the highest current, indicating a significant reduction in effective I_c given the modest B. Pancake #12 had no inductive response and behaved as a resistor with voltage linear to bus current. The joint voltages provide detailed examination on the altered current pathways in the TFMC, i.e., if

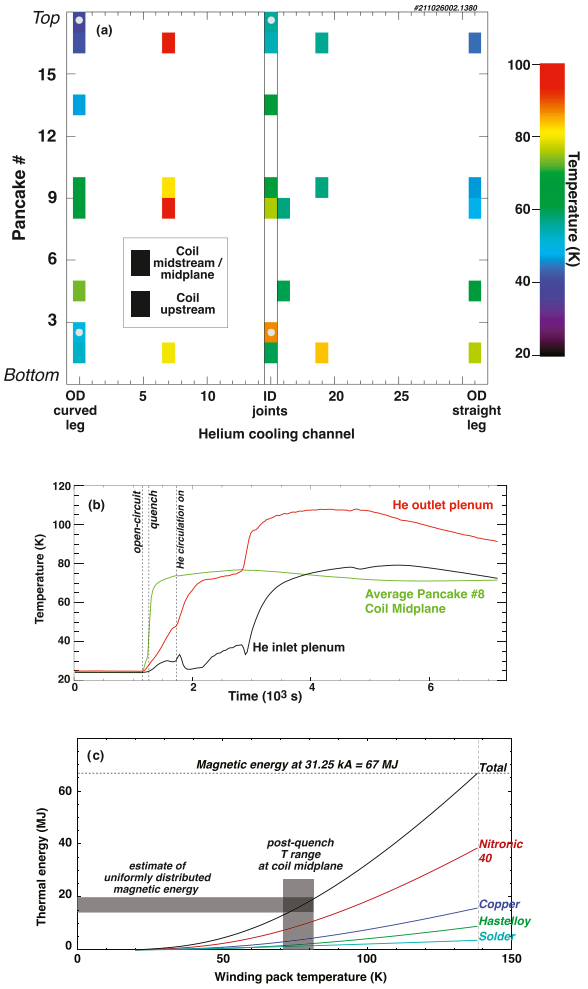

Fig. 20. Thermal evaluation of TFMC from the 31.5 kA triggered quench. (a) Temperature distribution in WP $\sim$ 100 s following quench (see Fig. 15 for plot description). (b) Sample temperature traces covering the open circuit, the quench, the restart of He coolant circulation, and 2-h postquench cooling. Helium coolant and inlet plena shown, and the average midplane temperature of pancake #8. (c) Distribution of thermal energy in WP component materials and total (structural case not included) as a function of temperature increase from initial $T = 24$ K assuming spatially uniform heating. Overlays show range of measured midplane WP postquench T and inferred estimate for fraction of 67 MJ of magnetic energy distributed uniformly in the WP by the quench.

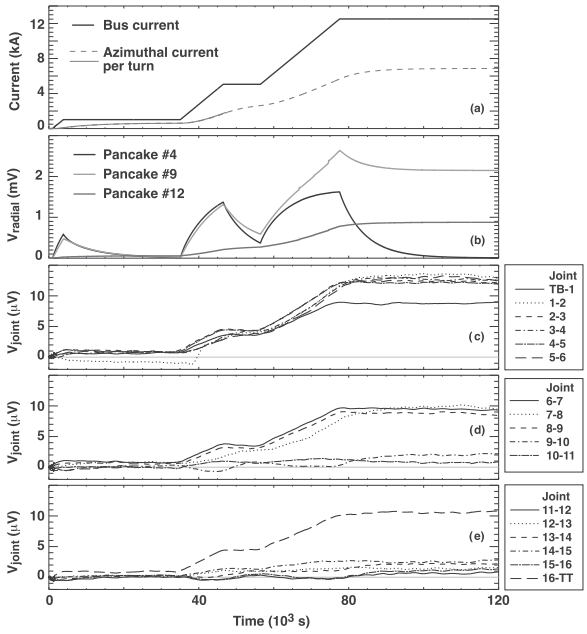

Fig. 21. Summary of EM testing at $T = 24$ K following the 31.5 kA quench (see Fig. 16) and recool. (a) Bus currents with I_{bus} flattops at 1, 5, and 12.5 kA. Overlaid azimuthal turn current (red) from FOCS (solid) and Teslameter (dashed) show effective loss of turns in the TFMC. (b) Pancake radial voltages for pancakes #4, #9, and #12. (c)–(e) Joint voltages indicating altered pancake-to-pancake current paths in upper half of WP and proper functioning of joints in lower half of WP with resistances $\sim 1 n\Omega$ similar to prequench values (see Fig. 7).

nominal voltages are not found on the joints, then the current continuity must be occurring in different locations indicating structural modifications to the pancake-to-pancake connections. From Pancakes #1–#9, the joints exhibit normal behavior with voltage linear to bus current (Pancake #1 is at the bottom of the coil). Indeed, the joint resistances are consistent with prequench values, indicating little to no damage. However, from Pancake #9–#16, there is little to no voltage indicating the current is not closing by turn currents. This is consistent with the loss of half the turns and B in the coil. The Pancake #16–top termination plate shows a normal joint voltage, consistent with the fact that the coil was not an open circuit.

The EM test, along with the thermal response, pointed to thermal damage in the top half of pancakes of the coil. The TFMC was disassembled to discern the details of the damage, a successful process made relatively clean and straightforward due to the demountable internal pancake-to-pancake joints and lack of VPI epoxy ground insulation present in insulated magnets. The visual inspection is summarized in Fig. 22 for the three pancakes exhibited in Fig. 21. Pancake #12 showed a clear "radial cut" with significant burn damage at the downstream tight corner. The solder and copper experience melting, indicating temperatures in excess of 1000 K being reached there. Similar damage was seen on adjacent pancakes, explaining the loss of ampere-turns in the coil, and the damage being localized in the downstream side is consistent with postquench thermal analysis. The local destruction of the REBCO superconductors is consistent with the pancake acting as a resistor in EM testing. Simple estimates of the relative volume burned (a few percent) in the TFMC were consistent with over 50% of the magnetic stored energy concentrating in this region. Pancake #9 did not burn, but the T exceeded the melt temperature of the solder 460 K. This is consistent with this pancake remaining superconducting but with degraded I_c due to the temperature excursion. Adjacent copper cap scarf-joints also showed signs of melting, presumably from insufficient electrical contact between cap sections during the current-in-copper phase of the quench where currents reached 100 kA. Pancake #4 showed no sign of burn, melt, or other mechanical damage at the corner or on the scarf joints. Subsequent LN_2 testing showed similar REBCO superconductor performance as prequench. The conclusion is that the bottom pancakes experienced rapid current distributions [see Fig. 19(c)] but were not affected by the Lorentz loading and out-of-groove

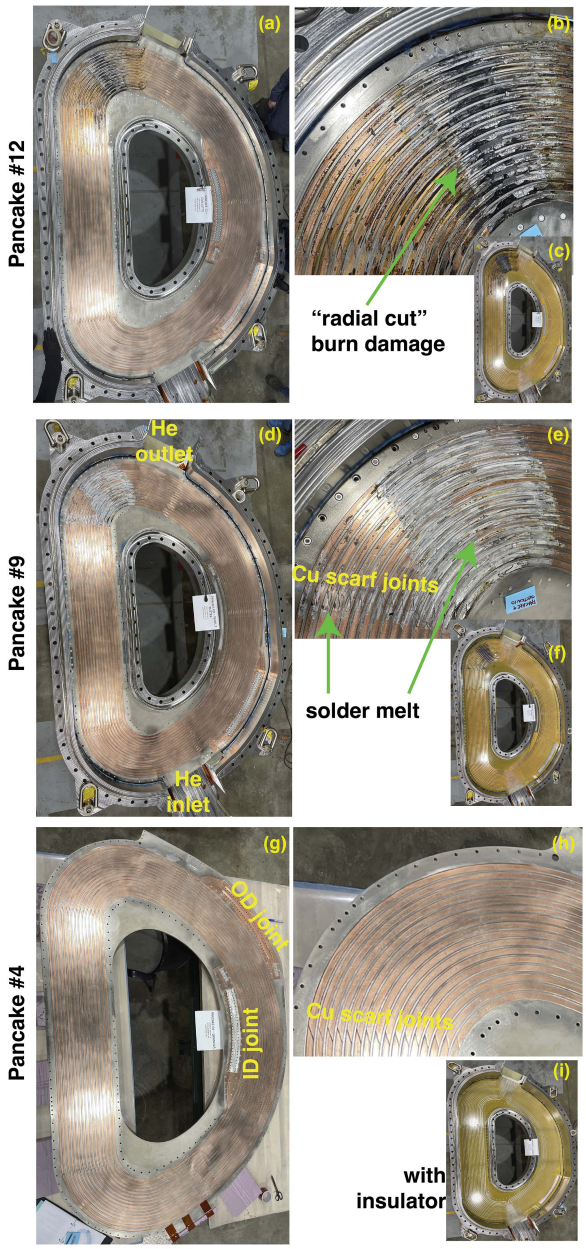

Fig. 22. Post open-circuit quench test photos of sample TFMC pancakes. (a)–(c) Pancake #12. (d)–(f) Pancake #9. (g)–(i) Pancake #4. Top of entire pancake viewing copper cap turns and radial plates (a) and (d) in the structural case and (g) removed from case. Location of He coolants inlet/outlet and joints labeled. Close-up photo of the downstream (near He outlet) high-B tight-turn corner with (b) showing burn damage from the quench "radial cut" (c) solder melting at the corner and on nearby scarf joints of the copper caps and (h) with no damage and pristine Cu scarf joints. Top view of pancakes with pancake-to-pancake electrical insulator in place (c), (f), and (i). The postquench voltage responses of these pancakes are shown in Fig. 21(b).

forces. This is consistent with the superconducting, charging, and flattop performance of the bottom coils in the TFMC. No other structural damage was identified in the TFMC pancakes or case.

The experimental results clearly align with the radial-cut hot spot results obtained by the nested-loop quench simulations [see Fig. 17(a)]. Subsequent comparisons of the simulations and data showed that, in fact, the mBS-dynamic model can/does produce the radial-cut result. This outcome required further refinement and tuning of the mBS simulations, including pancake I_c adjustments from the dc tests and the revision of joint resistances. Thus, the mBS model was not wrong *per se*, just highly sensitive to the detailed performance parameters of the coil. The details of these refined simulations are beyond the scope of this article and will be covered in forthcoming articles. Nonetheless, the results can be summarized in a general way. During the incubation phase, there is effectively a race between the global heating of the WP and the formation of a radial cut, and the "winner" depends on the details of how the heating is pushing the various parts of the WP through the REBCO superconducting critical surface. If the I/I_c (or T/T_c) surfaces are highly uneven, this favors a radial cut in the regions of high I/I_c, and furthermore, I/I_c can become localized by modifications to I_c; this evidently happened with Pancake #12 in the TFMC, which was at the epicenter of the radial cut. These lead to two important observations. First, the TFMC as-built was highly vulnerable to the radial cut because it *intentionally* used an uneven I/I_c design to achieve high B field in the tight-turn corner of a single coil in order to achieve the programmatic dc performance goals of $B > 20$ T. This design feature is less prominent in a TF coil set due to the field uniformity provided by the additional coils, but does not relieve the risk entirely according to models. Second, this points to a design strategy for avoidance of the radial cut by appropriate tailoring of I/I_c and control of the thermal trajectory of the WP through the critical surface. The details of this strategy are in a provisional patent [18] and will be covered in forthcoming articles.

IV. Discussion and Conclusion

The stated test goals for the TFMC were achieved.

1) *Confirm basic EM features of the coil such as radial resistance and inductance at resolution of the entire WP, pancake, and turn.* These features were found to be highly uniform and in excellent agreement with modeled values.
2) *Verify the superconducting state of REBCO stacks and quantify their performance compared to original REBCO tape performance and that found in liquid nitrogen pancake tests.* The REBCO tape stack superconductor performance could be captured with simple scalar corrections to critical current at the pancake level. Extrapolation from liquid nitrogen tests to high current/B and low-T conditions was satisfactory.
3) *Determine the resistance of pancake-to-pancake joints with varying currents, fields, and loads, which can only be measured in an assembled coil.* The joints had low and uniform resistance leading to low power dissipation 40 W at coil current over 40 kA and peak field of 20 T, providing deep thermal stability to the TFMC.
4) *Verify the structural integrity of the TFMC WP and case under varying loads.* The TFMC structural response was satisfactory under loading and unloading conditions with acceptable strain and mechanical stability of the pancakes and joints.

5) *Understand the dynamic response of the NINT TFMC to transient heating caused by open circuits of bus current.* The internal current circulation and resulting ohmic heating was verified and quantified with the successful suppression of high voltages and arcing and excellent agreement to simulations.
6) *Measure the quench dynamics and resiliency of the TFMC.* The model predictions of rapid inductive cascades for current redistribution in the pancakes were verified, as well as the eventual magnetic energy dissipation in the current-in-copper phase. A radial-cut hot spot developed in the high-B corner of the coil, which led to burn damage in that location comprising a small percentage of the coil volume. This provided necessary details to validate and benchmark quench simulations.

The SPARC programmatic goal of demonstrating a large-bore REBCO coil that could tolerate peak B fields > 20 were clearly achieved. Furthermore, the design strategy of using modular pancakes, connected by internal resistive joints, proved to be essential. In particular, this strategy allowed for quality checks of the pancake performance in liquid nitrogen prior to insertion into the coil. This check allows for quality assurance and predictive capability for dc performance of the full coil at high B and low T, features that will be essential in commercial-scale fabrication of such coils for fusion devices, including SPARC. A clear lesson learned from the tests was the value of lower current, high-T integrated coil tests. These tests revealed the accuracy limitations of using only liquid nitrogen test data (see Fig. 11) and allowed for important refinements of the models. Doing this test at low current decreases the operational risk to the coil due to the lower stored magnetic energy, while the relatively high T pushes down critical current to provide measurable dc voltages. It is, therefore, recommended for future integrated coil tests that the low-current high-T tests should be first and the results placed into the models.

A programmed open-circuit quench confirmed the details of a physics effect inside the coil, which should/can be avoided, i.e., a localized radial cut hot spot, by tailoring the critical current surface of the coil and controlling the thermal trajectory of the coil in the incubation phase. Besides the hot spot, the coil was generally self-protecting, avoiding high voltages and arcing, and with the REBCO tape stacks tolerating the rapid inductive quench with peak currents near 100 kA. It must be noted that an open circuit is not part of the normal operation of the coil; rather, this happens due to interruptions in power supplies to the coil. Furthermore, the coil responds on long timescales ($>$100 s) to the open circuit because it is thermally reacting to the volumetric heating from the internal circulating current. Therefore, facility design is most important in avoiding such quenches including redundancy in power supplies or rapid cooling capability. These strategies are being pursued for the use of NINT TF coils in SPARC.

Acknowledgment

The authors are indebted the following people: the entire TFMC team for their dedication and excellence; MIT Facilities, especially staff at the Central Utility Plant, for providing special cooling and power services for the TFMC test campaigns; MIT Environmental Health and Safety, especially Edward Lamere and Mitchell Galanek, for close collaboration on safety and procedures; the Safety and Operations Review Committee (George Dodson, Joseph Minervini, Edward Moses, and Soren Prestemon) for oversight and guidance of the test program; Jennifer James of MIT, who provided ceaseless 24-h support of the test team during the 20-T test campaign; and, finally, to our families who put up with not seeing any of us during the summer of 2021.

The magnet technology including the TFMC was developed as part of research collaborations between MIT and CFS and was funded by CFS. The parties have pursued patent protection relating to inventions created from their research collaborations and CFS has exclusive commercial rights to the technology for energy generation.

References

[1] Z. S. Hartwig et al., "VIPER: An industrially scalable high-current high-temperature superconductor cable," *Supercond. Sci. Technol.*, vol. 33, no. 11, 2020, Art. no. 11LT01.
[2] E. E. Salazar et al., "Fiber optic quench detection for large-scale HTS magnets demonstrated on VIPER cable during high-fidelity testing at the SULTAN facility," *Supercond. Sci. Technol.*, vol. 34, no. 3, 2021, Art. no. 035027.
[3] V. Fry, J. Estrada, P. C. Michael, E. E. Salazar, R. F. Vieira, and Z. S. Hartwig, "Simultaneous transverse loading and axial strain for REBCO cable tests in the SULTAN facility," *Supercond. Sci. Technol.*, vol. 35, no. 7, 2022, Art. no. 075007.
[4] B. Labombard, "Grooved, stacked-plate superconducting magnets and electrically conductive terminal blocks and related construction techniques," U.S. Patent 11 417 464, Aug. 2022.
[5] D. Whyte, "Small, modular and economically attractive fusion enabled by high temperature superconductors," *Philos. Trans. Roy. Soc. A*, vol. 377, no. 2141, 2019, Art. no. 20180354.
[6] A. Creely et al., "Overview of the SPARC tokamak," *J. Plasma Phys.*, vol. 86, no. 5, 2020, Art. no. 865860502.
[7] Z. Hartwig, R. F. Vieira, R. Leccacorvi, T. Toland, and D. Dunn, "The SPARC toroidal field model coil project," *IEEE Trans. Appl. Supercond.*, early access, Nov. 13, 2023, doi: 10.1109/TASC.2023.3332613.
[8] R. Vieira et al., "Design, fabrication, and assembly of the SPARC Toroidal Field Model Coil," submitted for publication.
[9] S. Hahn et al., "No-insulation multi-width winding technique for high temperature superconducting magnet," *Appl. Phys. Lett.*, vol. 103, no. 17, 2013, Art. no. 173511.
[10] T. Golfinopolous et al., "The testing facility for the SPARC Toroidal Field Model Coil," submitted for publication.
[11] J. Stillerman, T. Fredian, K. Klare, and G. Manduchi, "MDSplus data acquisition system," *Rev. Sci. Instrum.*, vol. 68, no. 1, pp. 939–942, 1997.
[12] T. Fredian, J. Stillerman, and G. Manduchi, "MDSplus extensions for long pulse experiments," *Fusion Eng. Des.*, vol. 83, nos. 2/3, pp. 317–320, 2008.
[13] J. De Launay, R. Dolecek, and R. Webber, "Magnetoresistance of copper," *J. Phys. Chem. Solids*, vol. 11, nos. 1/2, pp. 37–42, 1959.
[14] T. Mouratidis, "Low temperature solder demountable joints for non-insulated, high temperature superconducting fusion magnets," Ph.D. dissertation, Dept. Aeronaut. Astronaut., Massachusetts Inst. Technol., Cambridge, MA, USA, 2022.
[15] V. Fry et al., "50 kA capacity, nitrogen-cooled, demountable current leads for the SPARC Toroidal Field Model Coil," submitted for publication.
[16] P. Michaels et al., "A 20 K, 600 W cryocooler based supercritical helium circulation system for the SPARC Toroidal Field Model Coil Program," *IEEE Trans. Appl. Supercond.*, early access, Nov. 13, 2023, doi: 10.1109/TASC.2023.3332266.
[17] W. D. Markiewicz, T. Painter, I. Dixon, and M. Bird, "Quench transient current and quench propagation limit in pancake wound REBCO coils as a function of contact resistance, critical current, and coil size," *Supercond. Sci. Technol.*, vol. 32, no. 10, 2019, Art. no. 105010.
[18] B. LaBombard et al., "Heater-driven preemptive quench schemes for no-insulation superconducting magnets," U.S. Patent 63/514 704, Jul. 2023.